aerospace

MDPI

Article

Spacecraft Orbital Maneuver Detection Using Adaptive Multi-Feature Criteria

Shijie Zhai, Wenhua Cheng and Tinghua Zhang *

Department of Electronic and Optical Engineering, Space Engineering University, Beijing 101416, China; 15810887677@163.com (S.Z.); cwhcn@foxmail.com (W.C.)
* Correspondence: zth-gd@163.com

Abstract

To address the unstable detection of weak orbital maneuvers from publicly available Two-Line Element (TLE) data affected by natural perturbations, orbit-determination errors, outliers, and irregular update intervals, an adaptive multi-feature maneuver-detection method is proposed. The method incorporates a dominant J_2 perturbation correction into the computation of the mean semimajor axis and combines semimajor-axis variation, eccentricity variation rate, and local dispersion of mean motion. A two-stage outlier-processing scheme, iterative background-noise estimation, and an adaptive switching mechanism based on the sampling interval are further introduced. Multi-object simulations for low- and high-altitude satellites show that the average detection accuracies for along-track maneuvers are 94.47% and 93.95%, respectively, while those for radial maneuvers are 92.83% and 93.26%, respectively. The proposed method demonstrates stable detection performance and good applicability across different orbital altitudes and maneuver directions.

Keywords: orbital maneuver detection; multi-feature criterion; TLE time-series data

1. Introduction

With the rapid growth in the number of on-orbit spacecraft and the continued deployment of mega-constellations, orbital maneuvers have become an increasingly important factor affecting space-object state prediction, orbital cataloging, collision warning, and space traffic management. Maneuvers performed for station keeping, orbital transfer, or collision avoidance can induce discontinuous changes in orbital energy, geometry, plane orientation, or phase. Similar signatures, however, may also arise from natural perturbations, orbit-determination errors, and anomalous observations. Reliable discrimination among nominal orbital evolution, data anomalies, and genuine maneuvers in noisy orbital time series therefore remains a fundamental problem in space situational awareness. Two-Line Element (TLE) data provide broad target coverage, extensive historical archives, and low acquisition cost, making them an important publicly available data source for long-term monitoring of large populations of space objects. Lemmens and Krag investigated maneuver detection for low-Earth-orbit satellites using historical TLE sequences [1]. Li and Chen employed historical orbital data to monitor the operational status of LEO satellites [2], and Li et al. further extracted maneuver information from anomalous variations in orbital parameters [3]. Bai et al. applied clustering techniques to identify maneuver patterns in TLE data [4], while Clark and Lee combined orbital propagation with parallel processing to improve detection efficiency [5].

Check for updates

Academic Editor: George Z. H. Zhu

Received: 8 June 2026
Revised: 28 July 2026
Accepted: 6 August 2026
Published: 12 August 2026

Copyright: © 2026 by the authors. Licensee MDPI, Basel, Switzerland. This article is an open access article distributed under the terms and conditions of the Creative Commons Attribution (CC BY) license.

As research progressed, TLE-based maneuver detection evolved from simple orbital-element differencing toward more sophisticated perturbation modeling, statistical characterization, and robust anomaly detection. Mukundan and Wang detected maneuvers by comparing TLE variations with predictions from a simplified perturbation model [6]. Li and Chen used cluster analysis to identify space events from historical orbital data [7]. Song et al. investigated the sensitivity of semi-major-axis variations to orbital anomalies [8]. Shorten et al. combined SGP4 propagation with particle filtering for joint anomaly and maneuver detection [9]. Zhang et al. addressed TLE outliers and space-event detection using a multi-strategy genetic algorithm [10], whereas Liu et al. employed an expectation-maximization framework to characterize TLE errors and determine anomaly thresholds [11]. More recently, Liu et al. analyzed Starlink maneuvering strategies using mean orbital parameters derived from SpaceX-released ephemerides [12]. Gui et al. proposed a dual-moving-window curve-fitting method based on semi-major axis, eccentricity, and inclination, improving sensitivity to small-magnitude impulsive maneuvers in different directions [13]. These studies demonstrate the practical potential of historical orbital data, while also showing that detection performance remains sensitive to orbital-data noise, anomalous samples, feature construction, and threshold selection.

For targets with continuous high-precision observations, maneuver detection is often integrated with orbit determination and state estimation. Huang et al. developed a real-time robust method for detecting BeiDou GEO/IGSO maneuvers [14]. Tu et al. achieved real-time detection using epoch-differenced carrier-phase observations and broadcast ephemerides [15]. Qin et al. analyzed BeiDou maneuver characteristics using orbital elements [16], while Yu et al. investigated maneuver detection from a dynamical-model perspective [17]. Fan et al. combined orbital elements with satellite health information to identify BeiDou GEO/IGSO maneuvers [18]. Song et al. developed a near-real-time method based on triple-differenced carrier-phase observations [19], and Qin et al. used a square-root information filter to update orbital states and detect maneuvers [20]. Zhang et al. further embedded robust statistical detection into LEO real-time precise orbit determination and estimated velocity impulses in three orthogonal directions [21]. Qiao et al. combined residual analysis, kinematic orbit determination, and short-arc fitting to achieve automatic maneuver detection and thrust-model establishment for BeiDou GEO/IGSO satellites [22]. Although these approaches can provide high detection and estimation accuracy, they generally rely on continuous GNSS observations, broadcast ephemerides, or precise orbit products.

For non-cooperative targets, maneuver detection and estimation based on optical and radar observations have also been extensively investigated. Escribano et al. employed a stochastic hybrid-system framework for automatic maneuver detection and tracking in optical-survey scenarios [23]. Pastor et al. further studied maneuver detection and estimation using optical survey observations [24], and Porcelli et al. extended related techniques to radar-survey measurements [25]. Montilla et al. investigated maneuver detection for LEO objects using radar data [26], while Kaderali and Misra studied the detection and characterization of unknown spacecraft maneuvers [27]. Zhang et al. combined an extended Kalman filter for input detection and estimation with weighted nonlinear least squares to achieve near-real-time maneuver detection and estimation for non-cooperative targets [28]. Montilla et al. represented non-Gaussian uncertainty after long propagation intervals using Gaussian-mixture models and constructed corresponding radar-track maneuver metrics [29]. Yang et al. employed forward and backward nonlinear uncertainty propagation for maneuver confirmation and target association [30]. Pirovano and Armellin used convex optimization to detect and estimate maneuvers for space-object catalog maintenance [31]. These methods can make effective use of measurement residuals and orbital

dynamics, but their performance is constrained by sensor coverage, target visibility, and measurement accuracy.

The temporal characteristics of the data also have a direct impact on detection stability. Wu et al. proposed a wavelet-transform-combined-with-propagation method for low-data-rate conditions, fused semi-major axis and inclination into a composite detection criterion, and introduced a reconfirmation strategy to reduce false alarms [32]. For TLE data, the problem is further complicated by strongly nonuniform epoch intervals. Long intervals may amplify accumulated orbital-element variations, whereas very short intervals may artificially magnify time-normalized rates of change. Consequently, applying a uniform criterion across substantially different sampling intervals may lead to an imbalance among detection features.

Data-driven approaches have further expanded the methodological landscape of orbital maneuver detection. Xi et al. applied causal inference to GEO maneuver detection [33]. Li et al. used a convolutional neural network to identify station-keeping maneuvers of non-cooperative geosynchronous satellites [34]. Zollo and Weigel compared multiple maneuver-detection methods based on orbital-element timelines [35]. Yang et al. investigated passive maneuver detection for high-altitude targets using space-based optical observations [36], while Peng et al. developed a real-time LEO maneuver-detection method based on geometric-distance differences and dynamic thresholds [37]. Chen et al. employed a spiking neural network to extract temporal features from orbital data [38], and Cipollone et al. applied long short-term memory networks to support resident-space-object catalog maintenance [39]. Shi et al. proposed an adaptive spiking-gating multi-scale liquid-state machine for multi-scale feature fusion [40]. Ai et al. used an LSTM model to capture temporal dependencies in radar-based orbit-estimation residuals, thereby reducing false alarms and detection delay [41]. Although such approaches provide strong capability for learning complex temporal patterns, their performance generally depends on the availability and quality of labeled training data and on consistency between training and operational data distributions.

Despite substantial progress, maneuver detection from long-term publicly available TLE time series remains challenged by the dynamical consistency of mean orbital elements, contamination from anomalous observations, direction-dependent responses of orbital features, and nonuniform sampling intervals. To address these issues, this study proposes an adaptive multi-feature maneuver detection method. A J_2-based correction consistent with the SGP4 mean-element framework is first applied to recover the mean semimajor axis. The variations in semimajor axis, the rate of change of eccentricity, and the local dispersion of mean motion are then integrated to construct a composite detection criterion. In addition, outlier suppression, iterative background-noise estimation, and adaptive criterion switching based on the TLE epoch interval are incorporated to improve detection robustness across different orbital altitudes and under various in-plane maneuver conditions.

The remainder of this paper is organized as follows. Section 2 analyzes the responses of the orbital elements to natural perturbations and orbital maneuvers. Section 3 presents the proposed maneuver detection algorithm. Section 4 reports the experimental results and provides a detailed performance evaluation. Finally, Section 5 summarizes the main conclusions of this study.

2. Orbital Perturbations and Maneuver-Induced Responses of Orbital Elements

Under natural force fields, the orbital evolution of a space object is generally continuous and predictable. The forces acting on a spacecraft mainly include Earth's gravity and

orbital perturbations caused by the Earth's gravitational field, solar radiation pressure, atmospheric drag, and third-body gravity [42,43].

If a spacecraft is subjected to additional external forces or experiences abrupt disturbances in the space environment, its orbital evolution may deviate from this nominal behavior, manifesting as sudden changes in orbital parameters. Such additional forces can generally be classified into two types according to their acting duration: impulsive forces with extremely short durations, which can be approximated as instantaneous actions, and continuous low-thrust forces acting over relatively long durations. Both types of forces impart velocity increments to the object, thereby changing its orbital state [44–46]. The quantitative relationship between orbital parameter variations and velocity increments can be expressed by Equations (1)–(6):

$$\Delta a = \frac{2\sqrt{(1+2e\cos f+e^2)}}{n\sqrt{1-e^2}}dv_U \tag{1}$$

$$\Delta e = \frac{\sqrt{1-e^2}}{na\sqrt{(1+2e\cos f+e^2)}}[2(\cos f+e)dv_U - \sqrt{1-e^2}\sin E dv_N] \tag{2}$$

$$\Delta i = \frac{a(1-e\cos E)\cos u}{na^2\sqrt{1-e^2}}dv_W \tag{3}$$

$$\Delta\Omega = \frac{a(1-e\cos E)\sin u}{na^2\sqrt{1-e^2}\sin i}dv_w \tag{4}$$

$$\Delta\omega = \frac{\sqrt{1-e^2}}{nae\sqrt{(1+2e\cos f+e^2)}}\cdot[2\sin f dv_U + (\cos E+e)dv_N] - \cos i\Delta\Omega \tag{5}$$

$$\Delta M = -\frac{3n}{2a}\Delta a - \frac{1-e^2}{nae\sqrt{(1+2e\cos f+e^2)}}\left[(2\sin f + \frac{2e^2}{\sqrt{1-e^2}}\sin E)dv_U\right]\ (\cos E - e)\cdot dv_N] \tag{6}$$

In the above equations, a denotes the semi-major axis, which determines the orbital size and period; e denotes the eccentricity, which describes the orbital shape; f denotes the true anomaly, which specifies the satellite position along the orbit; and E notes the eccentric anomaly, which is related to the true anomaly and is used in the computation of Δe. The argument of latitude is defined as $u = \omega + f$, representing the position angle in the orbital plane and used in the calculation of Δi. In addition, dv_U, dv_N, and dv_W denote the tangential, radial, and normal velocity increments, respectively. According to Equation (1), the variation in the semi-major axis is mainly determined by the tangential velocity increment. Since the semi-major axis directly reflects the orbital mechanical energy and orbital scale, acceleration along the velocity direction increases the orbital energy and enlarges the semi-major axis, whereas deceleration in the opposite direction reduces the orbital energy and decreases the semi-major axis. Therefore, the semi-major axis is one of the most sensitive orbital elements for identifying in-plane orbital maneuvers, especially along-track maneuvers. Equation (2) indicates that the variation in eccentricity is affected by both tangential and radial velocity increments. Eccentricity characterizes the orbital shape. When a spacecraft is subjected to an in-plane velocity increment, the distribution of the perigee and apogee is adjusted, resulting in a change in eccentricity. Compared with the semi-major axis, eccentricity is more sensitive to radial velocity increments. Therefore, when weak maneuvers or maneuvers occurring at special orbital geometries are difficult to identify using the semi-major axis alone, the eccentricity variation rate can serve as an effective complementary feature. Equations (3) and (4) describe the variations in orbital inclination and right ascension of the ascending node, respectively. Their mathematical forms show that both quantities are directly related only to the normal velocity increment.

This indicates that changes in the orientation of the orbital plane are mainly caused by out-of-plane maneuvers and are weakly related to purely in-plane tangential or radial maneuvers. Therefore, if an orbital plane adjustment occurs, the inclination and right ascension of the ascending node will exhibit significant responses [47]. However, for the in-plane maneuvers mainly considered in this study, Δi and $\Delta\Omega$ are generally not the primary discriminative quantities. Equation (5) gives the relationship between the variation in the argument of perigee and the velocity increment. The argument of perigee describes the orientation of an elliptical orbit within the orbital plane, and its variation is jointly affected by tangential and radial velocity increments as well as the change in the right ascension of the ascending node. For in-plane maneuvers, $\Delta\omega$ reflects the rotation of the orbital shape within the orbital plane. For maneuvers involving a normal velocity increment, the argument of perigee is also indirectly influenced by $\Delta\Omega$ because of the rotation of the orbital plane. Equation (6) describes the variation in mean anomaly. The mean anomaly reflects the phase state of the spacecraft along its orbit. Its variation is not only related to the change in the semi-major axis but is also affected by tangential and radial velocity increments. Since a change in the semi-major axis modifies the orbital period and mean motion, the target phase may gradually deviate from the original orbit prediction after a maneuver, even when the orbital shape changes only slightly [48]. This characteristic indicates that orbital maneuvers may not only cause instantaneous jumps in orbital elements but also lead to the continuous accumulation of subsequent orbital phase errors.

3. Spacecraft Orbital Maneuver Detection Algorithm

3.1. J_2-Corrected Semi-Major Axis Computation for the TLE Mean Element System

The TLE data contain information such as the satellite number, orbital inclination, right ascension of the ascending node, eccentricity, argument of perigee, and mean anomaly. However, the semi-major axis is not directly provided. Under the assumption that orbital perturbations are neglected, the semi-major axis can be accurately computed from the mean motion parameter n_0 contained in the TLE data, together with Kepler's third law, as expressed in Equation (7):

$$a_1 = n_0^{-\frac{2}{3}} \tag{7}$$

The relationship between the mean motion n and the initial semi-major axis a_1 under the condition that perturbing forces are neglected can be obtained from Kepler's third law, where the gravitational constant is normalized. However, this value represents only the orbital parameter in the two-body problem and does not account for the influence of the J_2 orbital perturbation. Therefore, the J_2 perturbation correction factor δ_1 is introduced, and its calculation is given by Equation (8):

$$\delta_1 = \frac{3}{4}\frac{J_2}{a_1^2}\frac{(3\theta^2 - 1)}{\beta^3} \tag{8}$$

In the above equation, the first-order perturbation factor for the initial semi-major axis a_1 is defined. Here, the J_2 term denotes the second zonal harmonic coefficient of the Earth's gravitational field and is used to characterize the nonspherical gravitational effect caused by the Earth's equatorial bulge. The parameter $\theta = \cos i$ reflects the modulation of the perturbation strength by the corrected inclination, while $\beta = \sqrt{1 - e^2}$ represents the effect of eccentricity on the orbit-averaging process. Therefore, the magnitude of δ_1 depends not only on the initial semi-major axis, but also on the orbital-plane geometry and eccentricity.

Subsequently, based on Equation (8), a higher-order perturbation correction is applied to the semi-major axis a_1, yielding the corrected intermediate variable a_0. Its expression is given in Equation (9):

$$a_0 = a_1\left(1 - \frac{1}{3}\delta_1 - \delta_1^2 - \frac{134}{81}\delta_1^3\right) \tag{9}$$

The second-order expansion of δ_1 is adopted in the above equation, indicating that the influence of the J_2 perturbation is not treated as a simple linear perturbation. Instead, the nonlinear accumulation effect of the perturbation term during the inversion of the mean semi-major axis is further considered. Compared with Equation (14), a_0 is no longer a purely Keplerian orbital element, but an intermediate value of the mean semi-major axis corrected for the principal perturbation.

Subsequently, a second perturbation correction factor, δ_0, is introduced, whose expression is given in Equation (10):

$$\delta_0 = \frac{3J_2(3\theta^2 - 1)}{4a_0^2\beta^3} \tag{10}$$

In the above procedure, the correction factor is re-estimated using the semi-major axis a_0 obtained after the first correction, yielding a more consistent correction term δ_0. This process corresponds to a single-step correction iteration. Since δ_1 is computed based on the preliminary semi-major axis a_1, its accuracy is constrained by the initial-value error. After a more reasonable intermediate semi-major axis is obtained, recalculating the perturbation correction factor helps improve the matching accuracy between the mean motion and the semi-major axis. Therefore, δ_0 can more accurately represent the actual influence level of the J_2 perturbation under the current orbital configuration.

The newly obtained perturbation correction factor δ_0 is then used to correct the original TLE mean motion n_0, yielding the corrected mean motion n, as expressed in Equation (11):

$$n = \frac{n_0}{1 + \delta_0} \tag{11}$$

In Equation (11), the original TLE mean motion n_0 is corrected using the newly obtained perturbation correction factor, yielding the corrected mean motion n. This step is intended to ensure the internal consistency between the mean motion and the semi-major axis within the same mean element framework.

Finally, the mean semi-major axis is determined, and the corresponding solution procedure is expressed by Equation (12):

$$a = \frac{a_0}{1 - \delta_0} \tag{12}$$

The mean semimajor axis a is obtained from the intermediate quantity a_0 after application of the second-order correction factor. Compared with the initial estimate a_1, the resulting mean semimajor axis accounts for the combined effects of orbital inclination, eccentricity, and the dominant J_2 perturbation on the mean orbital scale, and is therefore more suitable for subsequent inter-epoch differencing of orbital elements. It should be emphasized that SGP4 is a standard analytical model for TLE-based orbit propagation, whose initialization and propagation procedures already account for the effects of the Earth's nonspherical gravity field, including the J_2 and J_4 terms, together with mean-motion recovery and secular and periodic corrections. The semimajor-axis treatment adopted in this study does not constitute a new perturbation model, nor is it intended to replace the complete SGP4 propagation procedure. Instead, for the purpose of maneuver detection, the mean semimajor axis is recovered at each TLE epoch using a mean-motion correction relationship consistent with the SGP4 initialization process, thereby maintaining compatibility with

the definition of TLE mean elements. Whereas standard SGP4 primarily propagates the orbital state to a specified epoch, the present approach extracts only the mean orbital scale at the TLE epochs and uses the inter-epoch semimajor-axis variation as a diagnostic feature of changes in orbital energy. This feature is subsequently integrated with the eccentricity variation rate and the local dispersion of mean motion. Accordingly, the contribution of this study does not lie in proposing new J_2- or J_4-correction formulas, but in incorporating an SGP4-consistent mean-element treatment into TLE time-series anomaly analysis and combining it with robust background estimation, outlier handling, and adaptive criterion switching under irregular sampling intervals to construct a physically interpretable multi-feature framework for detecting in-plane orbital maneuvers. Compared with direct semimajor-axis recovery based on the two-body Keplerian relationship, the adopted treatment mitigates the systematic bias in orbital scale caused by neglecting the dominant nonspherical-gravity effects; compared with the complete SGP4 model, it is used solely for detection-feature construction and does not involve orbit-state prediction, and therefore differs in both objective and scope. The overall computational procedure is illustrated in Figure 1.

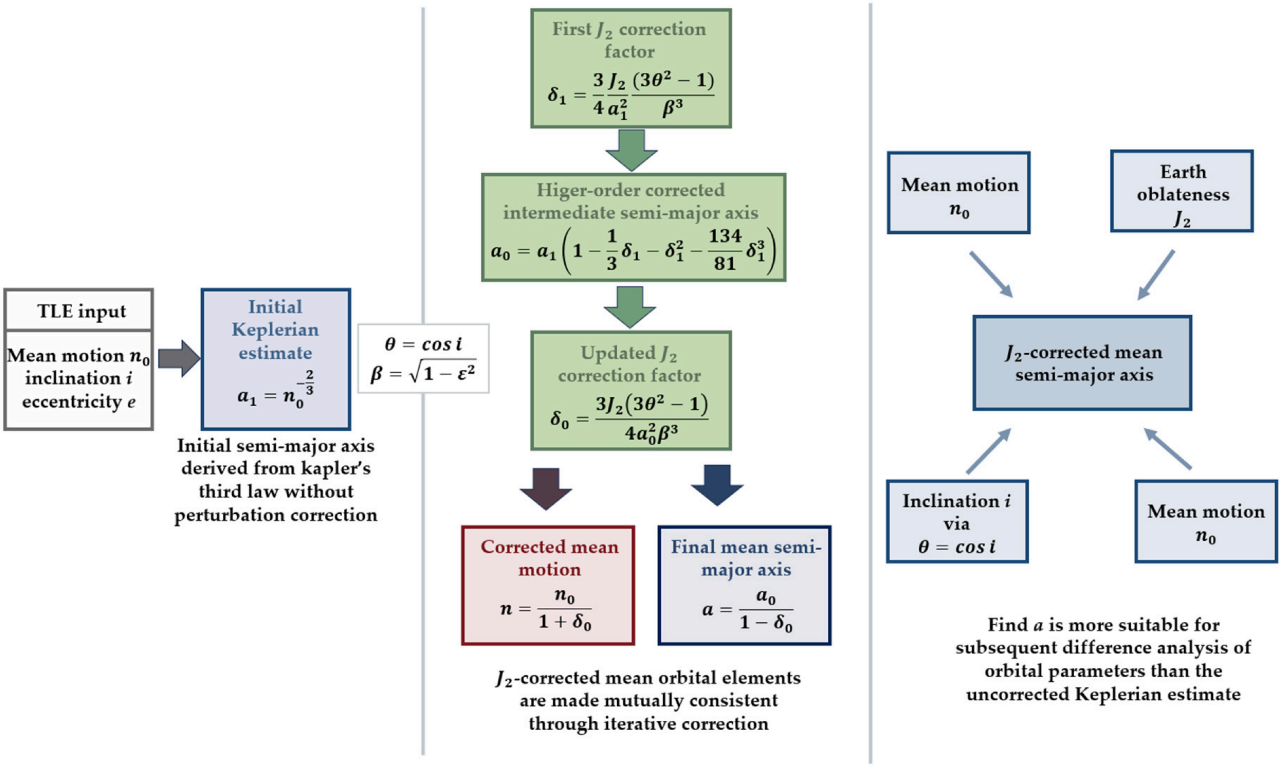


Figure 1. Flowchart of the Semi-Major Axis Computation.

3.2. Adaptive Multi-Feature Criterion for TLE Time-Series Data

After the mean semi-major axis has been computed from the TLE data, the continuous orbital element sequence must be further transformed into discriminative quantities capable of characterizing orbital maneuver signatures. Since in-plane orbital maneuvers usually induce local variations in orbital energy, orbital scale, and orbital shape, and the semi-major axis is highly sensitive to along-track velocity increments, the difference in semi-major axis between adjacent epochs can be used as an important feature for describing abrupt changes in the orbital state. However, the original TLE sequence is inevitably affected by observation errors, non-uniform data update intervals, and background fluctuations caused by natural perturbations. Directly applying a fixed threshold for anomaly discrimination may therefore

lead to false alarms or missed detections. Accordingly, based on the mean semi-major-axis sequence, this section develops an adaptive multi-feature composite criterion for TLE time-series data. By jointly analyzing the semi-major-axis difference, eccentricity variation rate, and mean-motion dispersion, the proposed criterion enables stable extraction and identification of anomalous features associated with orbital maneuvers. The detailed algorithmic steps are as follows:

Step 1: Within a specified time interval, the k TLE orbital element records are first arranged in ascending order of epoch. The mean motion parameter contained in each TLE record is then used to compute the corresponding mean semi-major axis, thereby obtaining the semi-major-axis sequence a_i. The difference in semi-major axis between two adjacent epochs is defined as follows:

$$\Delta a_i = a_{i+1} - a_i (i = 1, 2, 3, \cdots\cdots, k-1) \tag{13}$$

The original TLE orbital element sequence is transformed into a one-dimensional diagnostic sequence capable of characterizing in-plane maneuver behavior. Since the tangential impulsive thrust is approximately linearly related to the variation in the semi-major axis, the semi-major-axis difference sequence can sensitively reflect maneuver-induced changes in orbital energy.

Step 2: In orbital dynamics and space situational awareness, Two-Line Element data provide an important basis for orbit determination and orbital evolution analysis. However, owing to inherent errors in ground-based observation systems, noise introduced during data assimilation, and possible unmodeled perturbations associated with the target itself, the original TLE dataset inevitably contains a certain proportion of anomalous observations, namely outliers. Therefore, outlier removal is required.

In the initial data preprocessing stage, the primary objective is to extract the true and smooth long-term evolution trend of orbital elements, such as the semi-major axis, from the sample data used for statistical modeling. Given a sufficiently large dataset, the proportion of anomalous observations in the overall sample is usually limited. Therefore, this study adopts an empirical-threshold-based strategy. The samples are first sorted according to the magnitude of the semi-major-axis variation. For large-scale datasets, to improve processing efficiency and considering that outliers and anomalous points generally account for less than 5% of the total data under normal conditions, the top 5% of data points with the largest variation magnitudes are directly removed.

Then, a refined second-stage outlier removal is performed. At this stage, outliers typically appear as local sharp fluctuations in the resulting sequence that have no physical significance. The corresponding discrimination criterion is expressed in Equation (14):

$$\begin{cases} \Delta a_i \Delta a_{i+1} < 0 \\ \sqrt{(|\Delta a_{i+1}| - |\Delta a_i|)^2} < \beta |\Delta a_i| \end{cases} \tag{14}$$

Equation (14) is used to identify isolated spike-like gross errors in the semi-major-axis sequence. If the TLE mean elements at epoch $i+1$ are contaminated by an isolated orbit-determination gross error, while the adjacent epochs still approximately follow normal orbital dynamical evolution, the semi-major-axis sequence will typically exhibit a local "jump-and-return" anomaly. In this case, the adjacent differences Δa_i and Δa_{i+1} have opposite signs and approximately equal magnitudes. Therefore, the condition $\Delta a_i \Delta a_{i+1} < 0$ is used to determine whether the candidate point corresponds to a local reverse jump, whereas $\sqrt{(|\Delta a_{i+1}| - |\Delta a_i|)^2} < \beta |\Delta a_i|$ constrains the relative symmetry of the amplitudes before and after the jump. A real orbital maneuver generally changes the orbital energy, orbital scale, or orbital shape, causing the post-maneuver orbital elements to enter a new

sustained evolutionary state, rather than immediately returning to the original orbital level through a reverse change of approximately equal magnitude in the adjacent epoch. Therefore, Equation (14) is mainly used to remove single-point gross errors without sustained dynamical significance. In contrast, samples exhibiting a step-like variation trend, or accompanied by multi-feature-consistent anomalies such as changes in eccentricity variation rate and mean-motion dispersion, are retained for subsequent maneuver identification using the comprehensive criterion.

Here, β is a dimensionless relative amplitude tolerance coefficient, which characterizes the allowable relative asymmetry between the amplitudes of the "jump" and "return" stages. Therefore, when $\beta = 0.30$, the amplitude difference between two consecutive reverse jumps is constrained within 30%, requiring the local anomaly to exhibit a clearly identifiable approximately symmetric spike-like pattern. This value follows a relatively conservative gross-error rejection principle. If β is too small, only ideally symmetric single-point spikes can be identified, and gross errors with slight asymmetry caused by sampling-interval variations, short-period perturbations, and orbit-determination noise may be retained. Conversely, if β is too large, the local symmetry constraint will be excessively relaxed, increasing the risk that true weak maneuvers or boundary anomaly samples are incorrectly classified as single-point gross errors. Considering the nonuniform sampling characteristics of TLE data, the noise fluctuation in the semi-major-axis difference sequence, and the need to preserve true maneuver samples, β is set to 0.30 in this study, thereby achieving a compromise between isolated spike-like gross-error rejection and true maneuver-sample protection. It should be emphasized that β is used only in the preprocessing stage to identify candidate gross errors that strongly conform to an isolated spike-like pattern, and is not directly used as an orbit-maneuver detection threshold. Samples that do not satisfy this local symmetry condition, or that exhibit sustained step-like changes and multi-feature consistent anomalies in subsequent epochs, are retained for maneuver identification using the subsequent comprehensive criterion.

Step 3: For the data after outlier removal, the mean value of the semi-major-axis differences is calculated as expressed in Equation (15):

$$\Delta\overline{a} = \frac{1}{k-1}\sum_{k}^{k-1}|\Delta a_i| \tag{15}$$

The standard deviation is denoted by $\sigma_{\overline{a}}$, and its expression is given in Equation (16):

$$\sigma_{\overline{a}} = \sqrt{\frac{1}{k-2}\sum_{i}^{k-1}\left(|\Delta a_i| - \Delta\overline{a}\right)^2} \tag{16}$$

The initial orbital threshold is computed according to Equation (17):

$$\delta_a = \Delta\overline{a} + \lambda\sigma_{\overline{a}} \tag{17}$$

where the semimajor-axis variations under non-maneuvering conditions are assumed to arise primarily from intrinsic TLE uncertainties and nominal perturbation effects. Here, $\Delta\overline{a}$ and $\sigma_{\overline{a}}$ characterize, respectively, the mean variation amplitude and dispersion of the background sequence after outlier preprocessing, while λ is a scale-adjustment coefficient. Based on the parameter-sensitivity analysis, λ is set to 3 in this study. Continuous or slowly varying orbital responses induced by nominal perturbations are retained in the background sample set, whereas samples that substantially exceed the current background scale are temporarily excluded only during iterative threshold estimation. The resulting threshold is used to scale the semimajor-axis feature, while the final maneuver decision is made using a

composite criterion comprising semimajor-axis variation, eccentricity variation rate, and local dispersion of mean motion. The influence of nonuniform epoch intervals is further mitigated through the subsequent interval-adaptive switching mechanism.

Step 4: Classify the spacecraft according to its orbital altitude. Spacecraft with orbital altitudes below 2000 km are generally considered to be in low Earth orbit (LEO), whereas those with orbital altitudes above 2000 km are considered to be in medium Earth orbit (MEO) or high Earth orbit (HEO). For spacecraft with orbital altitudes below 2000 km, set $d = 0.005$ km; for spacecraft with orbital altitudes above 2000 km, set $d = 0.105$ km. If $\sigma_{\overline{a}} \geq d$ in Equation (16), the outlier-removed values $|\Delta a_i|$ obtained in Step 2 are compared with the initial threshold δ_a derived in Step 3. If $|\Delta a_i| \geq \delta_a$, then $\Delta a_i = \Delta\overline{a}$, and $\Delta\overline{a}$, $\sigma_{\overline{a}}$, and δ_a are recalculated according to Step 3.

The main purpose of Step 4 is as follows. If $\sigma_{\overline{a}}$ calculated in Step 3 is greater than the preset orbital-altitude-dependent threshold, it indicates that the current sample set contains large-amplitude jumps caused by actual orbital maneuvers. In this case, Δa_i values whose absolute values exceed this threshold are temporarily removed. If actual maneuver samples are directly included in the background and noise statistics, they will inflate the standard deviation and cause the threshold to deviate from the non-maneuver background. Therefore, by excluding these large-jump samples, this step approximates the distribution of pure background fluctuations. This treatment is particularly important for high-altitude spacecraft, for which the inherent errors in TLE data are relatively large. Hence, an empirical convergence constraint related to orbital altitude must be introduced to avoid threshold distortion.

Step 5: Repeatedly perform Steps 3 and 4 until $\sigma_{\overline{a}} < d$ is satisfied. The final threshold for orbital maneuver detection is then defined as $\delta_a = \Delta\overline{a} + 3 \cdot \sigma_{\overline{a}}$.

This step is essentially a robust statistical estimation procedure. By iteratively removing large-amplitude samples that may be caused by orbital maneuvers, the background-noise statistics gradually converge. The resulting threshold can therefore be regarded as a reasonable upper-bound estimate of the natural semi-major-axis fluctuations and TLE data errors within the considered time interval. Rather than relying on a single estimation result, the iterative correction process adaptively refines the threshold and improves the robustness of the algorithm against outliers. This is particularly important for practical orbital sequences involving multiple maneuvers with different maneuver magnitudes.

Step 6: The orbital parameters are calculated from sequential TLE data, yielding the following quantities. $|\Delta e/\Delta t|$ denotes the absolute rate of change in orbital eccentricity, where Δt represents the time interval between two adjacent sets of orbital elements. The parameter dn denotes the discrete ratio of the orbital mean motion. Physically, dn characterizes the deviation of the latest orbital elements of the target from its recent historical elements in terms of the mean motion n. Specifically, the most recent m mean-motion values of the target, for example, 15 values, are selected and arranged in reverse chronological order as $n_1, n_2, \cdots, n_m$. Based on these values, a specific calculation is performed for every three adjacent mean-motion values to obtain this parameter. The standard calculation procedure is described as follows:

$$c_i = \frac{1}{3}(n_i + n_{i+1} + n_{i+2}) \tag{18}$$

$$\eta = \sqrt{\frac{1}{3}\left[\left(\frac{n_i}{c_i} - 1\right)^2 + \left(\frac{n_{i+1}}{c_i} - 1\right)^2 + \left(\frac{n_{i+2}}{c_i} - 1\right)^2\right]} \tag{19}$$

$$\Delta\eta_j = |\eta_{i+1} - \eta_i| \tag{20}$$

$$dn_1 = \Delta\eta_1 / \frac{\sum_{j=1}^{m-3} \Delta\eta_j}{m-3} \tag{21}$$

In the above equation, $i = 1, 2, 3, \cdots, m-2$ and $j = 1, 2, 3, \cdots, m-3$. When $dn \approx 1$, the local fluctuation near the current epoch is close to the historical average level, indicating no evident anomaly. When $dn > 1$ and increases significantly, the local discrete variation near the current epoch is stronger than the nominal level, suggesting a higher probability of anomaly occurrence. When $dn \gg 1$, the latest orbital elements exhibit a pronounced discontinuity relative to the adjacent historical elements, which can be regarded as an important indicator of an orbital anomaly or orbital maneuver. Therefore, dn serves as a local statistical anomaly indicator that complements the criterion based on a single variation magnitude.

Step 7: Assume that m data groups are ultimately selected as the reference segment for orbital maneuver detection. Three thresholds, δ_1, δ_2, and δ_3, are then defined, and their calculation methods are given as follows:

$$\begin{cases} \delta_1 = \delta_a \\ \delta_2 = \max\left(\left|\frac{\Delta e_j}{\Delta t_j}\right|\right) \\ \delta_3 = \max\left(|dn_j|\right) \end{cases} \tag{22}$$

Where $j = 1, 2, 3, \cdots, m$. After the three sub-thresholds are calculated, the composite criterion corresponding to the i-th data point is defined as follows:

$$\delta_i = \frac{1}{3}\left(\frac{|\Delta a_i|}{\delta_1} + \frac{|\Delta e_i / \Delta t_i|}{\delta_2} + \frac{dn_i}{\delta_3}\right) \tag{23}$$

For the i-th data point, $\frac{|\Delta a_i|}{\delta_1}$ denotes the normalized absolute variation in the orbital semi-major axis at the i-th epoch. This term is mainly used to characterize the level of the current semi-major-axis variation relative to the upper bound of its nominal variation. $\frac{|\Delta e_i / \Delta t_i|}{\delta_2}$ denotes the normalized value of the eccentricity-rate sub-criterion at the i-th epoch, where $|\Delta e_i / \Delta t_i|$ is the absolute rate of change in eccentricity and is used to describe how rapidly the eccentricity changes per unit time between two adjacent epochs. Δt_i denotes the time interval between any two adjacent sets of satellite TLE data. $\frac{dn_i}{\delta_3}$ denotes the normalized value of the mean-motion discrete ratio dn_i, where dn_i measures whether the local dispersion of the mean-motion sequence near the current epoch significantly deviates from the historical nominal level. The introduction of this term not only reflects the magnitude and rate of change of the orbital elements themselves, but also captures the local statistical anomalies in the orbital-parameter sequence. The primary purpose of the composite criterion is to integrate multiple criterion quantities that characterize orbital anomalies from different perspectives into a single evaluation metric, thereby improving the stability and reliability of orbital maneuver detection. Compared with methods that rely on a single criterion, the composite criterion provides a more comprehensive representation of orbital-state variations, reduces false alarms caused by fluctuations in a single parameter, and improves the capability to identify complex orbital maneuvers or local anomalous events.

Step 8: For most samples satisfying $\Delta t \in [\Delta\bar{t}/5, 5\Delta\bar{t}]$, the composite criterion δ_i is used for anomaly identification, with the corresponding anomaly threshold set to 1. Here, $\Delta\bar{t}$ denotes the average update interval, which is a reference value calculated from the raw data. Physically, it represents the reciprocal of the average update frequency of the target data. For samples with significantly large time intervals, namely $\Delta t > 5\Delta\bar{t}$, the composite criterion is no longer used. Instead, criterion δ_2, which is more suitable for this type of data characteristic, is adopted, with $|\Delta e / \Delta t|$ used as the discriminating quantity.

If $|\Delta e/\Delta t|$ for a large-time-interval data point exceeds the threshold δ_2, it is classified as anomalous; otherwise, it is regarded as normal. Similarly, for samples with significantly small time intervals, namely $\Delta t < \Delta\bar{t}/5$, $|\Delta a|$ is used as the discriminating quantity. If $|\Delta a|$ for a small-time-interval data point exceeds the threshold δ_1, it is classified as anomalous; otherwise, it is classified as normal.

The rationale for setting the upper and lower bounds of the time interval and selecting the corresponding classification method is as follows. First, when $\Delta t > 5\Delta\bar{t}$, the sample time interval is significantly large. In this case, the accumulated value of $|\Delta a|$ may far exceed the normal level. Considering that $|\Delta a|$ accounts for one third of the weight in the composite criterion, this may lead to an imbalance in the composite criterion. Therefore, in this scenario, the absolute eccentricity variation rate $|\Delta e/\Delta t|$ is used as the indicator for anomaly identification, as it can more accurately reflect the true variation characteristics of the data. When $\Delta t < \Delta\bar{t}/5$, the excessively small sample time interval may cause the accumulated value of $|\Delta e/\Delta t|$ to increase significantly and even greatly exceed the normal value. Since this indicator also accounts for one third of the weight in the composite criterion, it may exert a large influence on the overall criterion and thereby reduce the stability of the composite criterion. In this case, using the absolute semi-major-axis variation $|\Delta a|$ as the discriminating quantity is more appropriate and can effectively improve the reliability of anomaly identification. Therefore, the time interval is restricted to the range $\Delta t \in [\Delta\bar{t}/5, 5\Delta\bar{t}]$ as the applicable interval for the composite criterion. This ensures that each component contributes to the overall criterion within a reasonable range and improves the stability and accuracy of the anomaly identification results. The schematic diagram is shown in Figure 2.

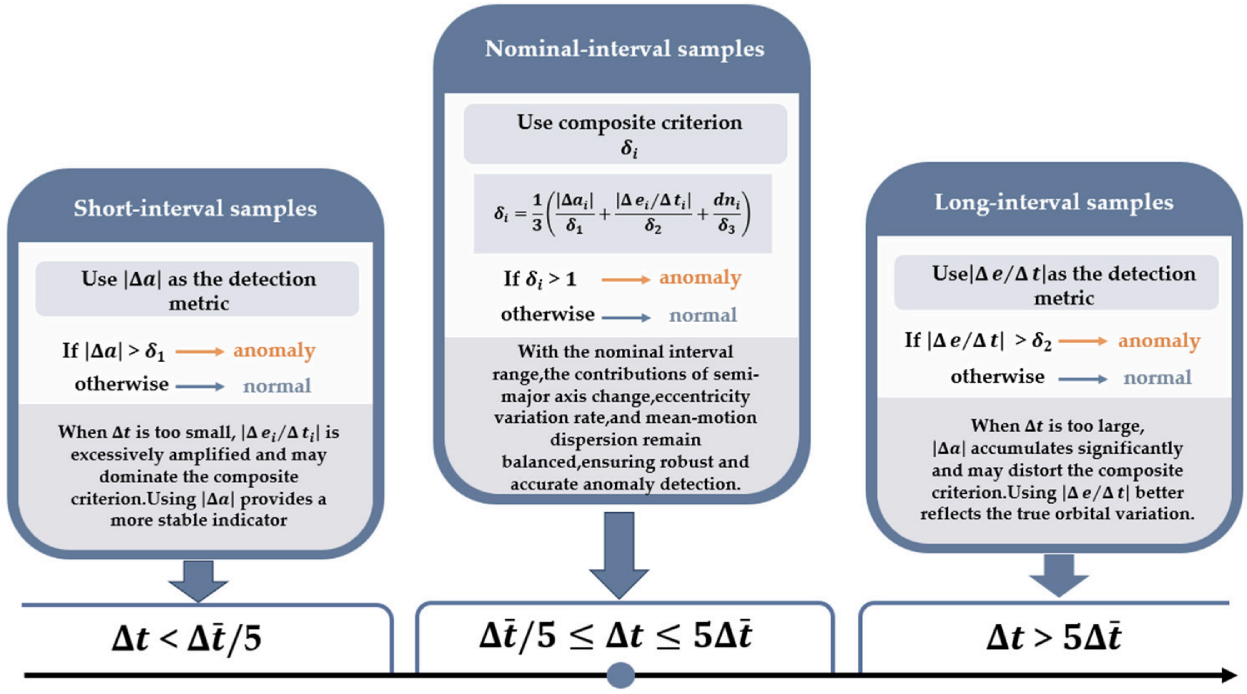


Figure 2. Adaptive criterion-switching mechanism for orbital maneuver detection using non-uniformly sampled TLE time-series data.

The complete orbital maneuver detection workflow is shown in Figure 3.

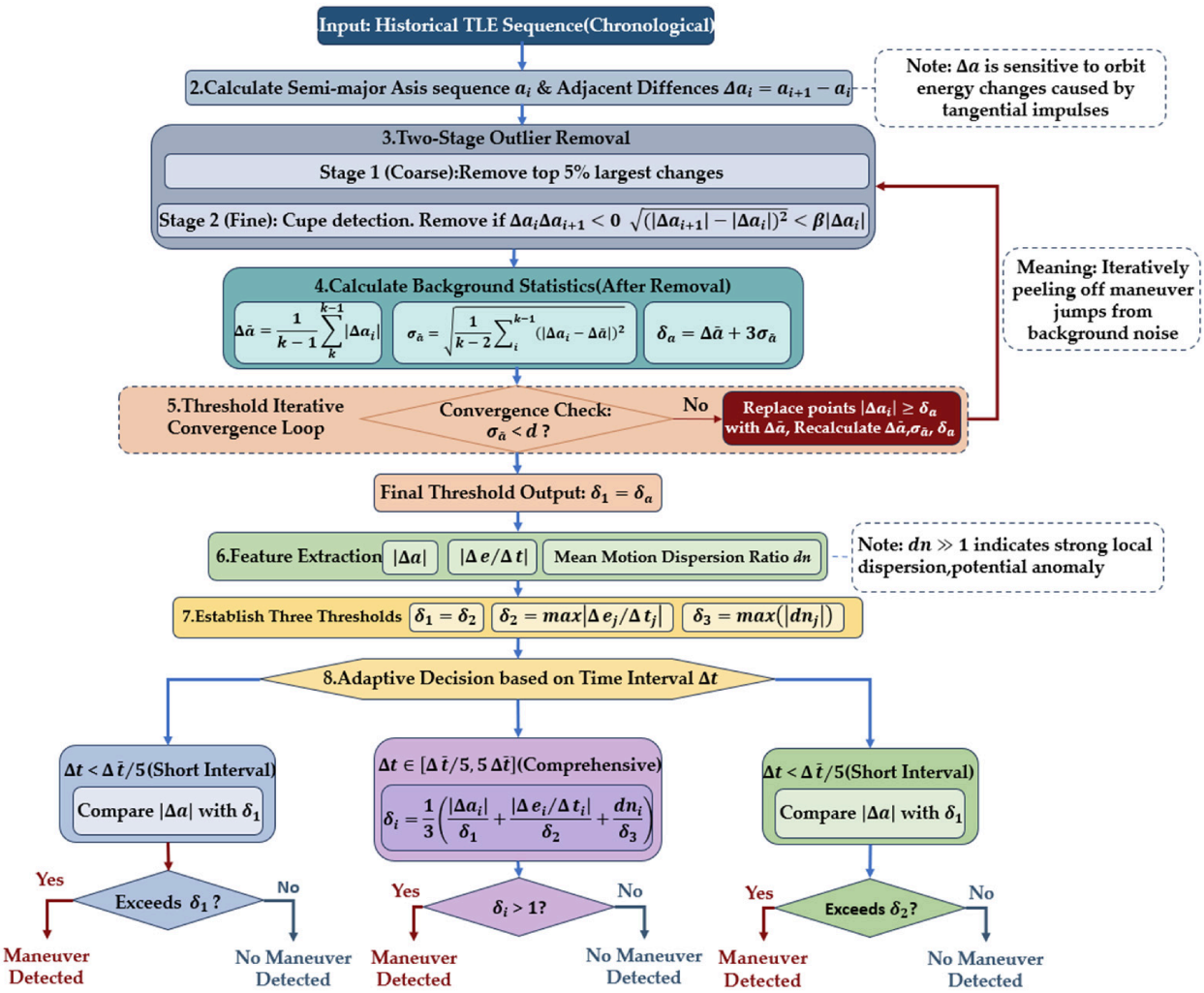


Figure 3. Overall workflow of spacecraft orbital maneuver detection.

3.3. Detection of Spacecraft Orbital Maneuver Epochs

In spacecraft orbital maneuver detection, it is necessary not only to determine whether an anomalous maneuver has occurred, but also to accurately identify the specific maneuver epoch. To this end, this study adopts a differential analysis method based on forward and backward propagation to identify the maneuver epoch and compute the orbital velocity increment. Given the spacecraft state vector at the initial epoch t_{k-1}, including the position vector $\vec{r}_{k-1}(t_{k-1})$ and velocity vector $\vec{v}_{k-1}(t_{k-1})$, as well as the state vector at epoch t_k, including the position vector $\vec{r}_k(t_k)$ and velocity vector $\vec{v}_k(t_k)$, forward propagation is performed from t_{k-1}. Specifically, the spacecraft orbital dynamics model is used to integrate the orbital state forward in time. The predicted position and velocity at an arbitrary epoch $t_{k-1} + \Delta t_i$ are denoted as $\vec{r}_{k-1}(t_{k-1} + \Delta t_i)$ and $\vec{v}_{k-1}(t_{k-1} + \Delta t_i)$, respectively. The orbital dynamics model used for forward propagation can be formulated using the standard Keplerian equations of motion:

$$\frac{d\vec{r}}{dt} = \vec{v} \tag{24}$$

$$\frac{d\vec{v}}{dt} = -\frac{\mu}{\left|\vec{r}\right|^3}\vec{r} + \vec{a}_{pert} \tag{25}$$

In the above equation, μ denotes the Earth's gravitational parameter, and $\vec{a}_{pert}$ denotes the perturbing acceleration, including the perturbations caused by Earth's nonspherical

gravitational field, atmospheric drag, solar radiation pressure, and third-body gravitational forces. Backward propagation is performed from t_k using the same dynamical model to integrate the orbital state backward in time. The predicted position and velocity vectors at an arbitrary epoch $t_{k-1} + \Delta t_i$ are denoted as $\vec{r}_k(t_k + \Delta t_j)$ and $\vec{v}_k(t_k + \Delta t_j)$, respectively. Backward propagation enables an effective comparison with the forward-predicted results. In particular, when a spacecraft undergoes an abrupt orbital adjustment, the state vectors obtained from the two propagation directions exhibit significant deviations, thereby indicating a potential anomalous maneuver.

The state vectors obtained from forward and backward propagation are compared. When the position deviation satisfies the following condition, the satellite is determined to have experienced an orbital anomaly at epoch $t_{k-1} + \Delta t_i = t_k - \Delta t_j$.

$$\begin{cases} \left|\bar{r}_{k-1}(t_{k-1} + \Delta t_i) - \bar{r}_k(t_k - \Delta t_j)\right| < \Delta r \\ t_{k-1} + \Delta t_i = t_k - \Delta t_j \end{cases} \tag{26}$$

In Equation (26), Δr denotes the allowable threshold for the position deviation, which is typically specified according to the orbital measurement accuracy. When the above condition is satisfied, the forward- and backward-predicted positions at this epoch are considered to be in good agreement, with the deviation remaining within the allowable range. Therefore, the spacecraft can be determined to have undergone an orbital maneuver at this epoch.

After the orbital maneuver epoch is determined, the velocity difference can be computed using the two propagation approaches, thereby obtaining the velocity increment associated with the orbital maneuver:

$$\Delta v = \left|\bar{v}_k(t_k - \Delta t_j) - \bar{v}_{k-1}(t_{k-1} + \Delta t_i)\right| \tag{27}$$

In Equation (27), Δv denotes the velocity change of the spacecraft at the maneuver instant. $\bar{v}_k(t_k - \Delta t_j)$ denotes the velocity vector obtained by backward propagation, whereas $\bar{v}_{k-1}(t_{k-1} + \Delta t_i)$ denotes the velocity vector obtained by forward propagation. The quantity Δv can be used to quantitatively evaluate the magnitude of the orbital adjustment caused by the orbital maneuver, thereby providing fundamental data for subsequent orbital control and anomaly analysis.

4. Results and Discussion

4.1. Natural Evolution of Orbital Elements Under an HPOP Perturbation Environment for Maneuver Detection

In this study, high-precision orbital simulations of the target satellite were performed using STK 12.2 (Systems Tool Kit). STK is a comprehensive software platform widely used for space mission design, orbital dynamics analysis, space-system modeling, and mission visualization. It enables satellite orbit propagation, maneuver modeling, orbit and attitude parameter output, and two- and three-dimensional mission scenario visualization within a unified time-varying space environment, thereby providing reliable simulation support for evaluating orbital maneuver effects. In the simulations, the HPOP (High Precision Orbit Propagator) was adopted as the orbit propagator to fully account for multiple perturbation effects during satellite orbital evolution. To improve the reproducibility of the simulation experiments, the main force-model settings of the HPOP propagator are further specified as follows. The non-spherical Earth gravity perturbation was modeled using the EGM96 Earth gravity field model, with the spherical-harmonic expansion truncated to degree and order 70. Here, the degree and order represent the maximum degree of the spherical-harmonic expansion and the maximum order of the corresponding spatial variation terms,

respectively. Third-body gravitational perturbations from the Sun and the Moon were modeled as point-mass gravitational attractions. Atmospheric drag was modeled using the NRLMSISE-00 atmospheric density model. Solar radiation pressure was enabled in the HPOP force model and represented using a spherical solar radiation pressure model. These force-model settings were kept unchanged throughout the entire simulation interval. These perturbation effects can significantly influence the long-term evolution of satellite orbits and are particularly important for high-precision orbit prediction and orbital design analysis. The classical orbital elements obtained from the HPOP simulation at specified epochs provide reference data for subsequent orbital analysis and mission planning. The simulation results are expressed in UTCG, based on Coordinated Universal Time (UTC). The epoch interval extends from 04:00:00 on 24 March 2026 to 04:00:00 on 26 March 2026, and selected classical orbital elements of the target satellite are listed in Table 1.

Table 1. Partial Evolution Data of the Six Orbital Elements of the Target Satellite under the HPOP Perturbation Model.

Time (UTCG)	Semi-Major Axis (km)	Eccentricity	Inclination (deg)	RAAN (deg)	Arg of Perigee (deg)	Mean Anomaly (deg)
24 March 2026 04:01	6966.957	0.000091	50.300	360.002	95.741	268.002
24 March 2026 04:02	6966.815	0.000182	50.299	360.001	102.110	265.376
24 March 2026 04:03	6966.577	0.000271	50.298	360.001	108.449	262.779
24 March 2026 04:04	6966.247	0.000360	50.297	359.999	114.738	260.232
24 March 2026 04:05	6965.833	0.000447	50.296	359.999	120.942	257.770
24 March 2026 04:06	6965.343	0.000532	50.294	359.998	127.034	255.420
24 March 2026 04:07	6964.787	0.000614	50.292	359.997	133.007	253.190
24 March 2026 04:08	6964.175	0.000694	50.290	359.995	138.870	251.067
24 March 2026 04:09	6963.513	0.000769	50.288	359.994	144.641	249.038
24 March 2026 04:10	6962.812	0.000841	50.285	359.991	150.322	247.098
24 March 2026 04:11	6962.084	0.000907	50.283	359.989	155.901	245.259
24 March 2026 04:12	6961.343	0.000967	50.280	359.986	161.362	243.539
24 March 2026 04:13	6960.602	0.001020	50.278	359.982	166.686	241.955
24 March 2026 04:14	6959.875	0.001066	50.275	359.978	171.861	240.520
24 March 2026 04:15	6959.174	0.001103	50.273	359.974	176.877	239.243

The variations in the six orbital elements over the epoch interval from 04:00:00 on 24 March 2026, to 04:00:00 on 26 March 2026, are shown in the following figure.

As shown in the Figure 4, under the HPOP high-precision orbit propagation model, the six orbital elements of the satellite exhibit an evident evolution pattern characterized by the coexistence of short-period oscillations and long-term slow drift. Specifically, the semi-major axis and eccentricity show relatively regular periodic fluctuations over time, reflecting small variations in orbital energy and orbital shape under the combined effects of perturbations such as Earth's nonspherical gravitational field, third-body gravitational forces, solar radiation pressure, and atmospheric drag. The orbital inclination exhibits periodic oscillations accompanied by a slight long-term variation trend, indicating that the attitude of the orbital plane is not strictly constant. The right ascension of the ascending node (RAAN) varies relatively smoothly overall, mainly reflecting the long-term nodal precession of the orbital plane dominated by the J_2 term. In contrast, the argument of perigee and mean anomaly show more pronounced periodic fluctuations and angle-wrapping behavior, which are typical manifestations of the continuous evolution of orbital elements in a perturbation environment. The variations in orbital elements under HPOP perturbations are continuous, regular, and predictable, which is directly relevant to orbital maneuver detection. In essence, an orbital maneuver refers to an abrupt change in orbital parameters, or the emergence of a new post-maneuver trend, caused by an additional control force acting on the satellite over a short time interval. Therefore, maneuver detection must

be built upon an accurate characterization of the nominal evolution of orbital elements under natural perturbation backgrounds. Without fully accounting for the high-fidelity perturbation effects described by HPOP, natural drift, periodic oscillations, or angular discontinuities induced by perturbations may be misidentified as orbital maneuvers. Conversely, when the natural perturbation model is known, an uncontrolled reference orbit can be constructed, and maneuver signatures can be effectively identified by analyzing the residuals, rates of change, and discontinuity features between the observed orbital elements and the perturbation-predicted results. These signatures include abrupt increases or decreases in the semi-major axis, anomalous variations in eccentricity, and abnormal deviations in orbital-plane parameters caused by thrusting actions. Therefore, analyzing the evolution patterns of the six orbital elements under HPOP perturbations not only reveals the long-term operational characteristics of the orbit, but also provides an important theoretical basis for threshold setting and anomaly discrimination in subsequent orbital maneuver detection.

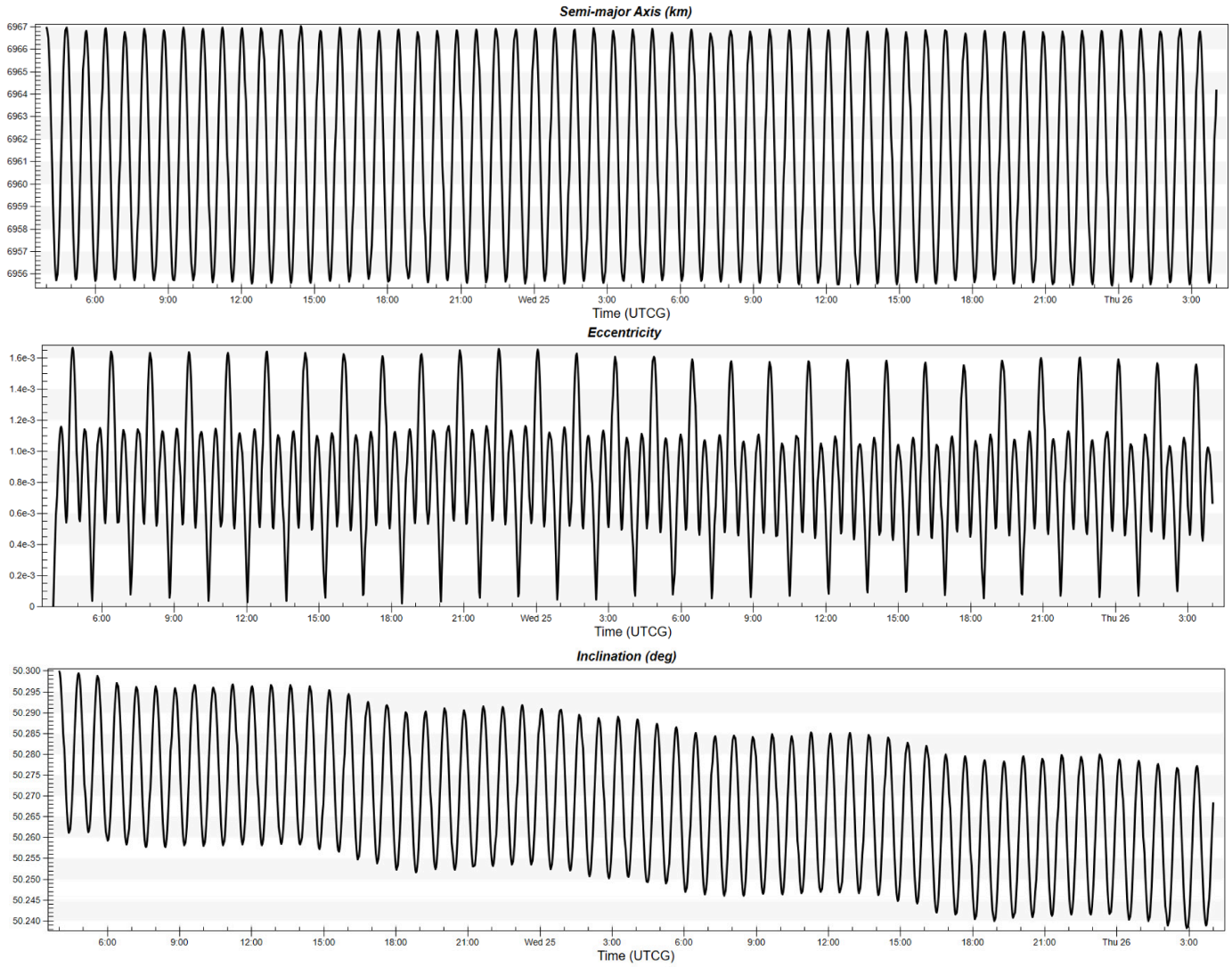


Figure 4. *Cont.*

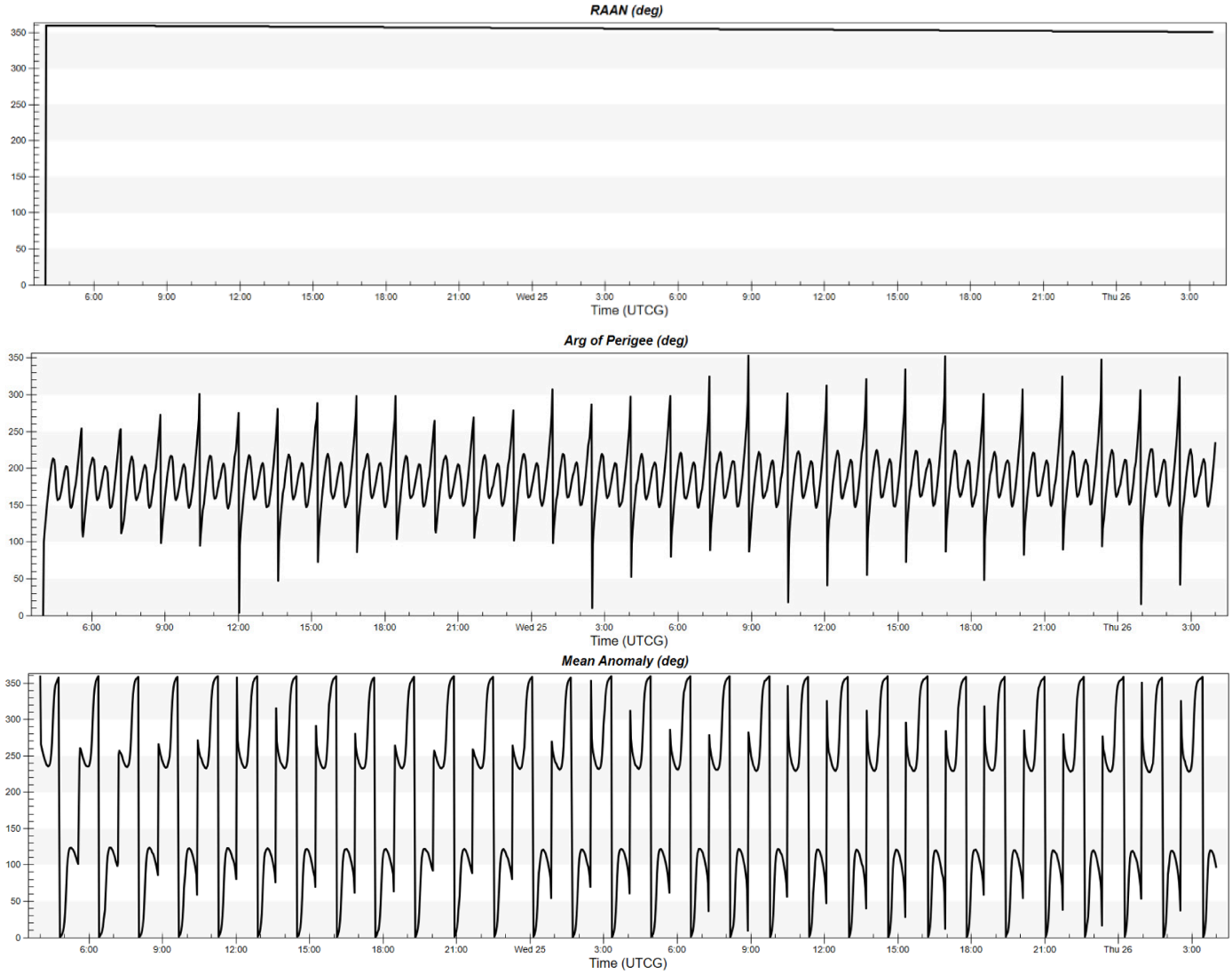


Figure 4. Time-Series Evolution Characteristics of Spacecraft Orbital Elements under a Perturbation Environment.

4.2. Analysis of the Impact of Single-Criterion Methods on Orbital Anomaly Identification

For the three orbital-anomaly indicators, a series of thresholds is determined for each indicator. When the orbital data exceed the corresponding threshold, the data point is classified as anomalous. To illustrate the independent application of the three anomaly indicators, TLE data from May 2023 for a subset of satellites with orbital altitudes ranging from 500 to 1200 km are used as an example. The interval false-alarm rate is defined as the proportion of data points incorrectly classified as anomalous within a given threshold interval relative to the total number of data points in that interval, excluding true anomaly cases. The missed-detection rate is defined as the proportion of actual orbital anomaly events that are not identified as anomalies among all orbital anomaly events. The three criterion components are then used independently for threshold-based detection, and the corresponding statistical results are presented in Tables 2–4.

As shown in Table 2, when the threshold for $|\Delta a|$ is relatively large ($>4 \times 10^{-1}$ km), the false-alarm rate becomes low (6.50%), whereas the missed-detection rate increases substantially to 54.50%. Conversely, when the threshold for $|\Delta a|$ is relatively small ($<1 \times 10^{-4}$ km), the system exhibits higher sensitivity, and the missed-detection rate decreases to 0%; however, the false-alarm rate becomes significantly higher.

Table 2. Orbital Maneuver Detection Analysis for Selected Satellites at Orbital Altitudes of 500–1200 km (Using $|\Delta a|$ as the Criterion).

$\lvert\Delta a\rvert$ Threshold (km)	Interval False-Alarm Rate (%)	Missed-Detection Rate (%)	$\lvert\Delta a\rvert$ Threshold (km)	Interval False-Alarm Rate (%)	Missed-Detection Rate (%)
$>4.0 \times 10^{-1}$	6.50	54.50	6.5×10^{-3}~8.0×10^{-3}	60.42	9.35
3.0×10^{-1}~4.0×10^{-1}	22.30	41.34	5.0×10^{-3}~6.5×10^{-3}	68.91	5.36
2.0×10^{-1}~3.0×10^{-1}	28.21	36.33	4.0×10^{-3}~5.0×10^{-3}	73.61	3.35
1.5×10^{-1}~2.0×10^{-1}	22.13	32.80	3.0×10^{-3}~4.0×10^{-3}	76.23	2.08
1.0×10^{-1}~1.5×10^{-1}	25.54	26.67	2.2×10^{-3}~3.0×10^{-3}	77.65	1.32
7.0×10^{-2}~1.0×10^{-1}	20.53	20.89	1.6×10^{-3}~2.2×10^{-3}	78.38	0.63
5.0×10^{-2}~7.0×10^{-2}	25.24	18.03	1.2×10^{-3}~1.6×10^{-3}	78.45	0.36
3.5×10^{-2}~5.0×10^{-2}	30.80	25.96	9.0×10^{-4}~1.2×10^{-3}	79.47	0.00
2.5×10^{-2}~3.5×10^{-2}	40.15	14.78	6.5×10^{-4}~9.0×10^{-4}	79.56	0.00
1.8×10^{-2}~2.5×10^{-2}	50.52	19.04	4.5×10^{-4}~6.5×10^{-4}	79.78	0.00
1.2×10^{-2}~1.8×10^{-2}	55.60	16.69	3.0×10^{-4}~4.5×10^{-4}	79.86	0.00
1.0×10^{-2}~1.2×10^{-2}	53.25	14.60	1.0×10^{-4}~3.0×10^{-4}	79.83	0.00
8.0×10^{-3}~1.0×10^{-2}	52.56	14.37	$<1.0 \times 10^{-4}$	79.89	0.00

Table 3. Orbital Maneuver Detection Analysis for Selected Satellites at Orbital Altitudes of 500–1200 km Using $|\Delta e/\Delta t|$ as the Criterion.

$\lvert\Delta e/\Delta t\rvert$ Threshold	Interval False-Alarm Rate (%)	Missed-Detection Rate (%)	$\lvert\Delta e/\Delta t\rvert$ Threshold	Interval False-Alarm Rate (%)	Missed-Detection Rate (%)
$>3.0 \times 10^{-3}$	14.57	50.76	1.2×10^{-3}~1.5×10^{-3}	46.20	25.90
2.5×10^{-3}~3.0×10^{-3}	20.36	48.29	9.0×10^{-4}~1.2×10^{-3}	48.82	20.36
2.0×10^{-3}~2.5×10^{-3}	30.21	42.35	6.0×10^{-4}~9.0×10^{-4}	52.36	15.21
1.8×10^{-3}~2.0×10^{-3}	33.58	38.96	3.0×10^{-4}~6.0×10^{-4}	60.59	10.83
1.5×10^{-3}~1.8×10^{-3}	37.86	35.62	$<3.0 \times 10^{-4}$	66.28	7.69

Table 4. Orbital Maneuver Detection Analysis for Selected Satellites at Orbital Altitudes of 500~1200 km Using dn as the Criterion.

dn Threshold	Interval False-Alarm Rate (%)	Missed-Detection Rate (%)	*dn* Threshold	Interval False-Alarm Rate (%)	Missed-Detection Rate (%)
>25	9.20	38.30	5~6	76.20	8.10
20~25	30.82	25.33	4~5	77.81	5.36
15~20	45.43	18.67	3~4	78.53	4.00
12~15	55.34	16.33	2~2.5	79.12	2.00
10~12	62.18	15.35	1.5~2	79.65	1.32
9~10	65.94	14.67	0.8~1.2	79.89	0.00
8~9	68.55	14.00	0.5~0.8	79.92	0.00
7~8	72.76	10.78	0.3~0.5	79.94	0.00
6~7	74.60	8.10	<0.3	79.85	0.00

As shown in Table 3, for the $|\Delta e/\Delta t|$-based criterion, when the threshold gradually decreases from 3.0×10^{-3} to below 3.0×10^{-4}, the interval false-alarm rate increases from 14.57% to 66.28%, whereas the missed-detection rate decreases from 50.76% to 7.69%. This indicates that reducing the decision threshold enhances the detector's sensitivity to small variations in orbital parameters, enabling it to identify more potential maneuver events. However, it also increases the likelihood that parameter fluctuations caused by the nominal perturbation background are included within the maneuver-detection range.

As shown in Table 4, when a relatively large threshold for dn is adopted ($dn > 25$) to achieve a lower false-alarm rate (9.20%), the detection sensitivity is compromised, resulting in a substantial fraction of true anomalies being missed, with a missed-detection rate of 38.30%. Conversely, when a stringent threshold is used ($dn < 0.3$) to ensure that all anomalies are captured, corresponding to a missed-detection rate of 0%, the system becomes overly sensitive and produces excessive false alarms, with a false-alarm rate of 79.85%. These results demonstrate the inherent limitations of fixed-threshold detection methods that rely on any single parameter.

As shown in Figure 5, the variations in the interval false-alarm rate and missed-detection rate under different thresholds are evaluated using $|\Delta a|$, $|\Delta e/\Delta t|$ and dn as single criteria. Overall, all three criteria exhibit a clear trade-off between the false-alarm rate

and the missed-detection rate. When the threshold is relatively high, the false-alarm rate remains low, whereas the missed-detection rate is high. As the threshold decreases, the missed-detection rate declines; however, natural perturbations, TLE data noise, and local fluctuations in orbital elements are more likely to be misclassified as anomalies, leading to an increased false-alarm rate. For the $|\Delta a|$ criterion shown in Figure 5a, when $|\Delta a| > 4.0 \times 10^{-1}$ km, the false-alarm rate is only 6.50%, whereas the missed-detection rate reaches 54.50%. As the threshold decreases, the missed-detection rate drops rapidly and approaches zero in the low-threshold range, while the false-alarm rate continues to increase. When the threshold is lower than 1.0×10^{-4} km, the false-alarm rate reaches 79.89%, indicating that this criterion is susceptible to noise and small orbital perturbations under low-threshold conditions. Figure 5b shows that the $|\Delta e/\Delta t|$ criterion exhibits a similar trend, with the missed-detection rate decreasing and the false-alarm rate increasing as the threshold decreases. When $|\Delta e/\Delta t| > 3.0 \times 10^{-3}$, the false-alarm rate is 14.57% and the missed-detection rate is 50.76%. When the threshold is lower than 3.0×10^{-4}, the false-alarm rate increases to 66.28%, while the missed-detection rate decreases to 7.69%. This indicates that although this criterion can reflect certain maneuver-related features, its stability is limited when used alone. Figure 5c demonstrates that the dn criterion is more sensitive to threshold variations. When $dn > 25$, the false-alarm rate is only 9.20%, but the missed-detection rate remains 38.30%. As the threshold decreases, the missed-detection rate gradually declines and approaches zero near $dn < 1.2$, whereas the false-alarm rate simultaneously increases to nearly 80%. This suggests that dn can characterize anomalies in orbital motion frequency and local statistical behavior, but it is prone to interference from propagation errors, short-period perturbations, and nonuniform TLE updates under low-threshold conditions.

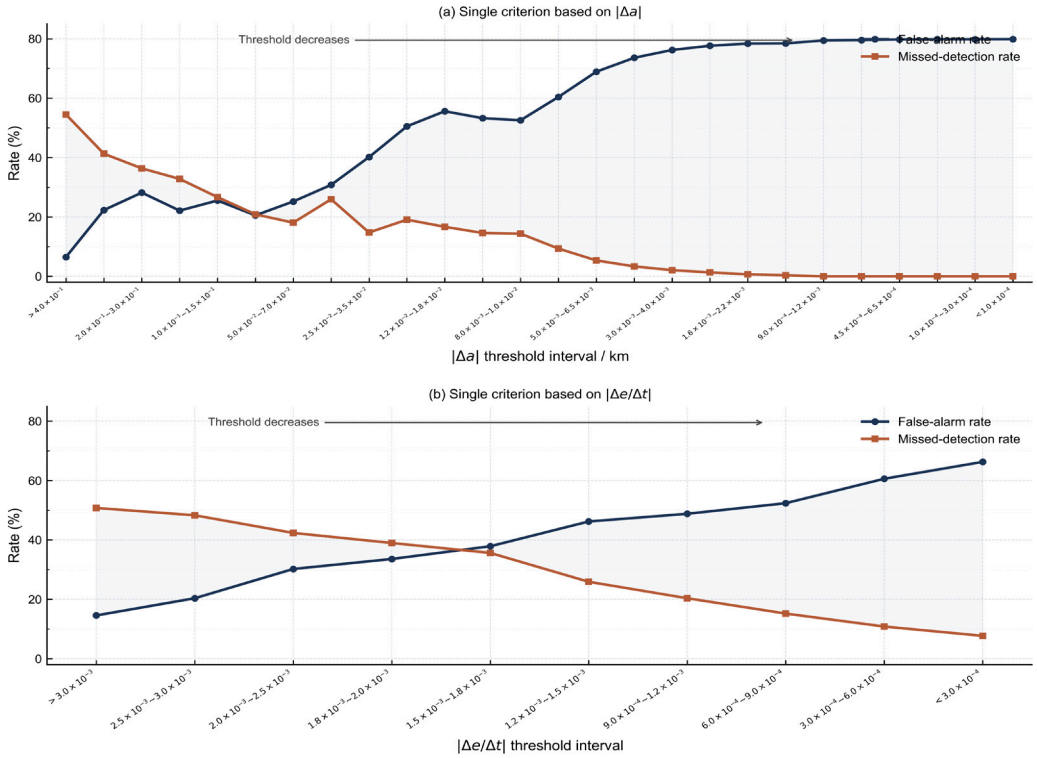


Figure 5. *Cont.*

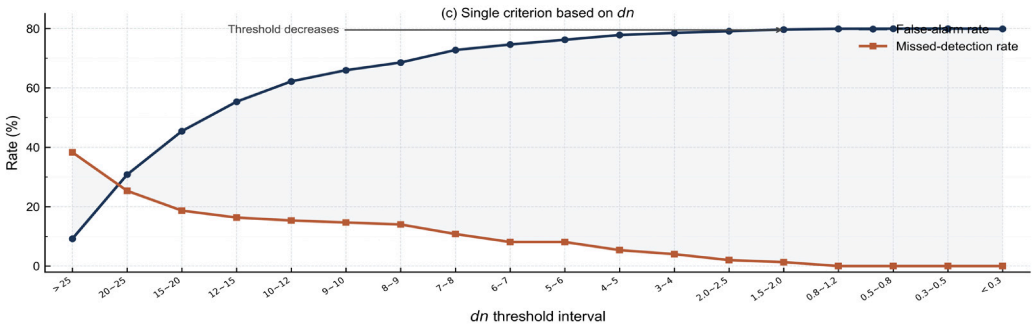


Figure 5. Trade-off Between the False-Alarm Rate and the Missed-Detection Rate under Threshold Variations of a Single Criterion. (**a**) Single criterion based on $|\Delta a|$. (**b**) Single criterion based on $|\Delta e/\Delta t|$. (**c**) Single criterion based on dn.

In summary, the three single criteria cannot simultaneously maintain low false-alarm and missed-detection rates over the entire threshold range. Higher thresholds weaken the ability to identify weak maneuvers, whereas lower thresholds amplify false alarms. Therefore, single fixed-threshold methods are difficult to adapt to orbit maneuver detection tasks under complex perturbation backgrounds, different orbital altitudes, and nonuniform TLE update conditions.

4.3. In-Plane Orbital Maneuver Detection Experiment for LEO Spacecraft

4.3.1. Along-Track Impulsive Maneuver Detection Experiment for LEO Spacecraft

To systematically analyze the influence of along-track impulsive maneuvers on the orbital dynamical characteristics of a low Earth orbit experimental satellite, this study uses STK to construct a satellite orbit simulation scenario and performs orbit propagation and parameter-evolution analysis. In the simulation, the initial semi-major axis of the experimental satellite is set to 7006.36 km, and the initial epoch is set to 25 March 2026 04:00:00.000 UTCG. At 43,200 s after the initial epoch, the first impulsive velocity increment is applied along the instantaneous velocity direction of the satellite, with a maneuver magnitude of 70 m/s. Subsequently, at 43,200 s after the completion of the first impulsive maneuver, a second impulsive velocity increment is again applied along the instantaneous velocity direction of the satellite, with a maneuver magnitude of 50 m/s. Based on the orbital dynamics propagation results obtained using STK 12.2, the time-series evolution characteristics of the satellite semi-major axis and eccentricity during the two-impulse along-track maneuver process are extracted and analyzed. The variation in the semi-major axis is shown in Figure 6, and the variation in eccentricity is shown in Figure 7. These simulation results can be used to reveal the influence of impulsive velocity increments along the velocity direction on the orbital energy, orbital scale, and orbital shape of the satellite, thereby providing theoretical and simulation support for subsequent orbital maneuver effect evaluation, orbital anomaly behavior identification, and maneuver strategy design.

As shown in Table 5, in the large-magnitude orbital maneuver scenario described above, the impulsive velocity increments applied along the satellite velocity direction significantly alter the orbital mechanical energy and orbital geometry. Consequently, both the semi-major axis and eccentricity exhibit pronounced abrupt or step-like changes before and after the maneuvers. The magnitudes of these changes are much larger than the background fluctuations caused by nominal orbital perturbations, numerical propagation errors, and observational noise, resulting in maneuver signatures with a high signal-to-noise ratio and clear temporal separability. The proposed orbital maneuver detection algorithm can stably capture anomalous variation features in the orbital-element sequence under such strong-maneuver conditions and accurately identify the corresponding maneuver epochs, with the overall detection success rate remaining close to 100%. These results indicate that,

when the dynamical response induced by an orbital maneuver is sufficiently significant, the proposed method can effectively distinguish true maneuver behavior from the slow orbital evolution caused by natural perturbation backgrounds, demonstrating good detection sensitivity and stability.

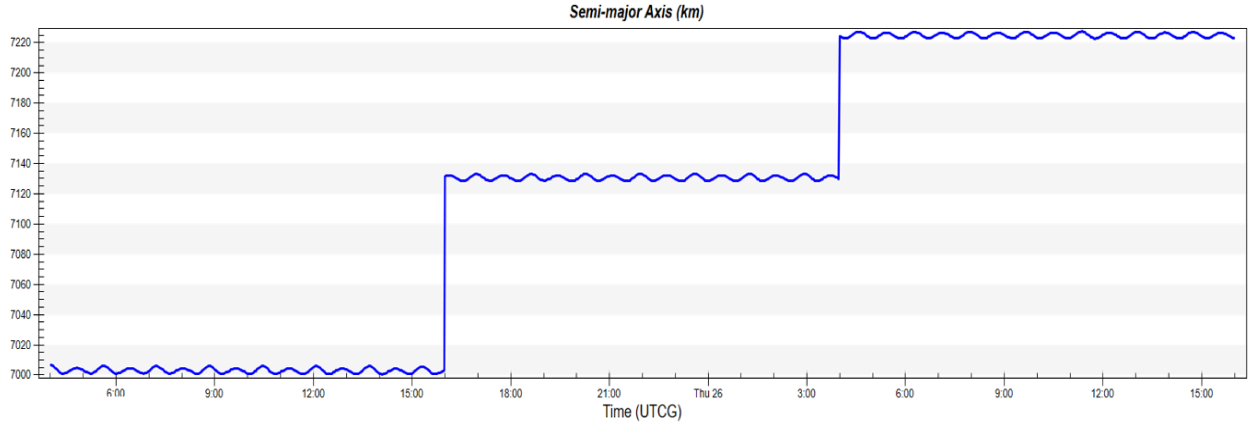


Figure 6. Variation in the Semi-Major Axis of a Low Earth Orbit Satellite after Two Orbital Maneuvers.

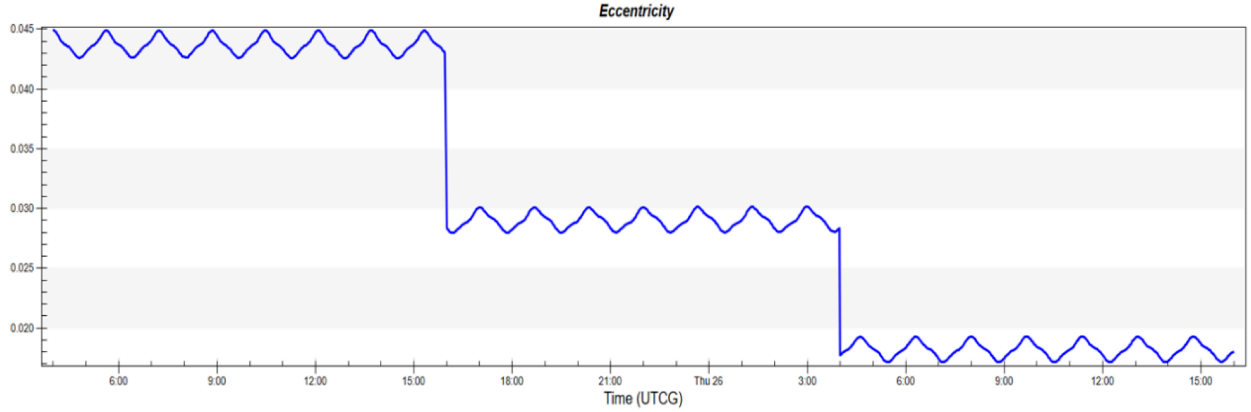


Figure 7. Variation in the Eccentricity of a Low Earth Orbit Satellite after Two Orbital Maneuvers.

Table 5. Partial Variation Data of Orbital Elements for a Low Earth Orbit Satellite after Two Maneuvers.

Time (UTCG)	Semi-Major Axis (km)	Eccentricity	Inclination (deg)	RAAN (deg)	Arg of Perigee (deg)	Mean Anomaly (deg)
25 March 2026 15:54:49	7002.442	0.043128	28.478	356.800	6.041	128.943
25 March 2026 15:56:05	7002.704	0.043050	28.480	356.796	6.021	133.621
25 March 2026 15:57:20	7002.959	0.042971	28.482	356.793	5.986	138.337
25 March 2026 15:58:36	7003.201	0.042893	28.484	356.79	5.937	143.09
25 March 2026 15:59:53	7003.424	0.042819	28.486	356.788	5.872	147.879
25 March 2026 16:00:00	7131.603	0.028376	28.486	356.788	25.315	128.842
25 March 2026 16:01:00	7131.765	0.028309	28.487	356.787	25.261	132.509
25 March 2026 16:02:16	7131.942	0.028227	28.489	356.786	25.169	137.212
25 March 2026 16:03:33	7132.079	0.028152	28.490	356.786	25.051	141.950
25 March 2026 16:04:50	7132.173	0.028085	28.490	356.786	24.910	146.718
25 March 2026 16:06:07	7132.226	0.028030	28.491	356.786	24.749	151.513
25 March 2026 16:07:24	7132.220	0.027988	28.490	356.786	24.571	156.330
26 March 2026 03:55:41	7130.484	0.028221	28.470	353.881	28.018	192.922
26 March 2026 03:56:58	7130.197	0.028278	28.467	353.876	27.917	197.681
26 March 2026 03:58:15	7129.912	0.028338	28.465	353.871	27.836	202.419
26 March 2026 03:59:33	7129.634	0.028397	28.463	353.865	27.772	207.136
26 March 2026 04:00:00	7224.084	0.017733	28.462	353.863	6.938	229.597
26 March 2026 04:01:00	7223.875	0.017782	28.460	353.857	6.937	233.142
26 March 2026 04:02:17	7223.625	0.017841	28.458	353.85	6.950	237.682
26 March 2026 04:03:34	7223.402	0.017894	28.456	353.842	6.975	242.203
26 March 2026 04:04:50	7223.211	0.017941	28.455	353.833	7.004	246.711
26 March 2026 04:06:07	7223.059	0.017983	28.454	353.824	7.033	251.206

However, in practical space-object monitoring and anomalous-behavior identification tasks, spacecraft orbital maneuvers do not always manifest as large-magnitude feature changes. Small-amplitude or weak maneuvers often induce only subtle perturbations in the orbital elements, with variation magnitudes that may be comparable to the levels of orbital perturbation noise or data uncertainty. This imposes higher requirements on the robustness of the detection algorithm and its capability to identify weak signals. To further extend the coverage of algorithm performance validation, this study constructs orbital maneuver simulation scenarios for multiple low Earth orbit satellites using STK. In this simulation scheme, several impulsive orbital maneuvers are configured for ten low Earth orbit satellites, whose orbital semi-major axes range from 6871 km to 8371 km. The maneuver direction is set along the instantaneous velocity direction of each satellite, and the maneuver velocity increments are randomly generated within the range of 0–10 m/s to simulate orbital evolution under weak maneuvers and different maneuver-intensity conditions. By statistically analyzing the detection results under multi-target, multiple-maneuver, and random small-amplitude velocity-increment scenarios, the applicability, interference resistance, and stable detection performance of the proposed algorithm under weak orbital-element variation backgrounds are further evaluated.

After determining the comprehensive criterion parameters for each target LEO satellite, it is necessary to further evaluate the applicability and stability of the selected parameter combination in practical anomaly-identification tasks. Table 6 first presents the threshold-parameter settings for the ten satellites, reflecting the parameter-selection characteristics of the comprehensive criterion method for different targets. The identifiers listed in the table are experimental IDs assigned in the simulation and are used solely to distinguish different simulated targets. On this basis, Figure 8 further summarizes the total number of data samples, the number of identified anomalous data points, the number of false detections, the number of missed detections, and the detection accuracy for each satellite, thereby quantitatively evaluating the detection performance of the constructed criterion system. In this study, the detection accuracy is used to evaluate the reliability of the identified anomaly samples, and is defined as the proportion of correctly identified anomaly samples after excluding misclassified samples from all identified anomaly samples. The number of missed detections is reported as an independent statistical item to characterize the completeness with which true maneuver-induced anomaly samples are captured, and is not included in the calculation of detection accuracy.

Table 6. Low Earth Orbit Satellite Numbers and Threshold Settings.

No.	Satellite ID	δ_1	δ_2	δ_3
1	27642	0.58	0.0158	5.94
2	28738	0.43	0.0132	6.52
3	29674	0.29	0.0173	5.61
4	30211	0.62	0.0127	9.86
5	30718	0.47	0.0165	8.89
6	31527	0.26	0.0142	6.18
7	31864	0.49	0.0133	5.33
8	32471	0.36	0.0157	4.68
9	32902	0.53	0.0146	6.97
10	33548	0.45	0.0166	7.32

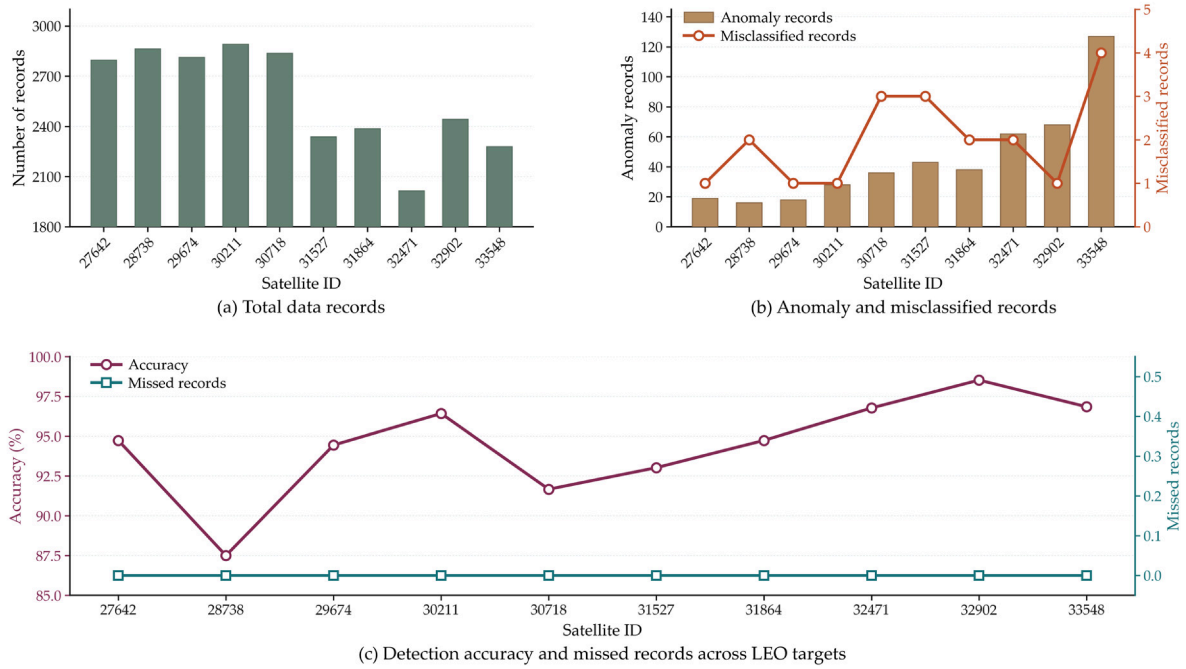


Figure 8. Orbit maneuver detection results for LEO satellites. (**a**) Total data records. (**b**) Anomaly and misclassified records. (**c**) Detection accuracy and missed records across LEO targets.

As shown in Figure 8, the orbit maneuver detection results of 10 LEO satellites were statistically analyzed. Figure 8a presents the number of TLE data samples for each target. The sample size of each satellite ranges from 2016 to 2891, with a total of 25,662 orbital data records, indicating that the experimental dataset is sufficiently large and that the data scales of different targets are generally comparable. Figure 8b shows the number of anomaly records identified for each satellite and the corresponding number of misclassified records. A total of 455 anomaly records were identified for the 10 satellites, among which 20 records were misclassified. The number of anomaly samples varies noticeably among different targets. Specifically, satellite 33548 has the largest number of anomaly records, reaching 127, while satellites 32902 and 32471 contain 68 and 62 anomaly records, respectively. Although the number of anomaly samples fluctuates considerably across different targets, the number of misclassified records for each target remains within the range of 1–4, indicating that the proposed method maintains good misclassification suppression capability under varying anomaly scales. Figure 8c presents the detection accuracy and the number of missed detections for each target. The results show that the number of missed detections is 0 for all targets, indicating that the proposed method can completely capture the known anomaly samples in this experiment. The detection accuracy of different satellites ranges from 87.5% to 98.5%, with an average accuracy of 94.47%. Among them, satellite 32902 achieves the highest detection accuracy of 98.5%, whereas satellite 28738 exhibits a relatively lower accuracy of 87.5%. This is mainly because satellite 28738 contains only 16 anomaly samples, and a small number of misclassified records therefore has a relatively pronounced influence on its accuracy. Overall, this experiment represents a typical low-anomaly-ratio and class-imbalanced detection scenario. These results demonstrate that the proposed algorithm can effectively suppress misclassifications under the background noise of TLE data while maintaining complete capture of true orbit-maneuver-induced anomaly samples, thereby validating its stability and reliability in LEO satellite orbit maneuver detection tasks.

4.3.2. Radial Impulsive Maneuver Detection Experiment for LEO Spacecraft

To further verify the applicability and generalization capability of the proposed method for in-plane orbital maneuvers dominated by radial velocity increments, an independent LEO radial impulsive maneuver simulation scenario is additionally constructed in this study. Different from the preceding along-track maneuver experiment, another set of ten LEO satellites is selected as the experimental targets, and their satellite catalog numbers do not overlap with those used in the along-track experiment, thereby avoiding dependence of the detection results on a specific target set. The semi-major axes of the selected satellites are controlled within the range of 6871~8371 km to ensure that their orbital altitude distribution is comparable to that of the previous LEO experiment. For each target satellite, orbit propagation is performed using the HPOP high-precision orbit propagator in STK 12.2. The perturbation force model, data output scheme, background noise estimation method, adaptive threshold calculation procedure, and multi-feature composite criterion are kept consistent with those used in the preceding experiments. In the simulation, several radial impulsive orbital maneuvers are assigned to each LEO satellite. The radial velocity increment is randomly generated within the range of 0~10 m/s, and the maneuver direction is randomly selected between the positive and negative radial directions to simulate weak radial maneuvers and the orbital element responses under different maneuver directions. To ensure comparability with the along-track impulsive maneuver experiment, the maneuver times are randomly selected within the effective observation interval and are prevented from being too close to adjacent maneuvers. During the detection process, the decision parameters are not readjusted for the radial maneuver experiment; instead, the same parameter determination procedure as in the previous experiments is adopted. To quantitatively evaluate the detection performance for LEO maneuvers dominated by radial velocity increments, the total number of data samples, number of anomalous samples, number of false alarms, number of missed detections, and detection precision are still used as statistical indicators. Figure 9 presents the detection results of ten LEO satellites under the radial impulsive maneuver scenario, which are used to further evaluate the proposed algorithm in terms of anomaly capture capability, false-alarm suppression capability, and detection stability for weak radial maneuver samples.

As shown in Figure 9, this study analyzes the orbit maneuver detection results of ten LEO satellites under radial-velocity-increment-dominated conditions. The ten LEO satellites contain a total of 25,567 orbital data records, with the number of records for each satellite ranging from 2174 to 2912, indicating a sufficient sample size. Figure 9a shows that the data volume varies among different target satellites, which enables the evaluation of the detection stability of the proposed algorithm across different LEO targets. Figure 9b shows that 597 anomaly records are identified in the radial impulsive maneuver scenario, accounting for 2.34% of the total samples. The number of misclassified records is 45, accounting for 0.176% of all samples. The number of misclassified records for each satellite ranges from 1 to 9. Among them, satellites No. 42829 and No. 39088 have relatively more anomaly records, with 104 and 92 records, respectively, indicating differences in the orbital responses of different targets to radial velocity perturbations. Figure 9c presents the detection precision and the number of missed records. In this study, detection precision is used to evaluate the reliability of the identified anomaly samples, while the number of missed records is listed as an independent statistical indicator and is not included in the calculation of detection precision. The results show that the detection precision of individual satellites ranges from 90.22% to 95.65%, with an average detection precision of 92.83%. The total number of missed records is 7, accounting for only 0.027% of all samples. Overall, the proposed adaptive multi-feature composite criterion maintains high detection precision, a low misclassification ratio, and a low missed-detection level in the radial

impulsive weak-maneuver scenario, verifying its applicability and stability for detecting radial in-plane maneuvers of LEO spacecraft.

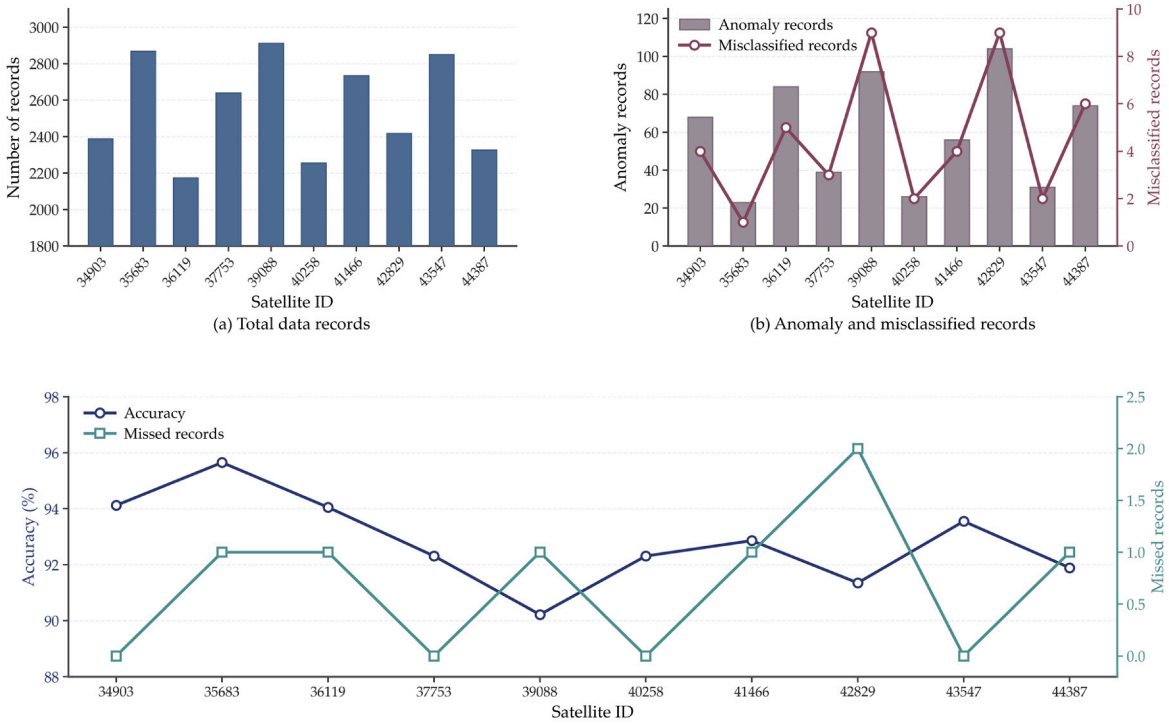


Figure 9. Detection results for ten LEO spacecraft under radial impulsive maneuver scenarios: (**a**) total number of orbital data records for each target satellite; (**b**) detected anomaly records and corresponding misclassified records; and (**c**) detection accuracy and missed records across different LEO radial-maneuver targets.

4.4. In-Plane Orbital Maneuver Detection Experiment for High-Orbit Spacecraft

4.4.1. Along-Track Impulsive Maneuver Detection Experiment for High-Orbit Spacecraft

To further analyze the influence of along-track impulsive maneuvers on the orbital dynamical characteristics of high-orbit experimental satellites, and to further validate the applicability of the proposed orbit maneuver detection method in high-orbit scenarios, a typical high-orbit satellite simulation scenario was constructed using STK, followed by orbit propagation and analysis of the evolution characteristics of the orbital elements. In the simulation, the initial semi-major axis of the experimental satellite was set to 42,164 km. This orbital scale is comparable to that of a typical geosynchronous orbit and can therefore reasonably represent the orbital dynamical characteristics of high-orbit satellites. The initial epoch was set to 25 March 2026 04:00:00.000 UTCG.

To investigate the influence of along-track velocity increments on the orbital elements of high-orbit satellites, two impulsive orbit maneuvers were configured in the simulation scenario. The first maneuver was performed 43,200 s after the initial epoch, along the instantaneous velocity direction of the satellite, with a velocity increment of 10 m/s. The second maneuver was performed 43,200 s after the completion of the first impulsive maneuver, also along the instantaneous velocity direction of the satellite, with a velocity increment of 20 m/s.

Based on the orbit-dynamics propagation results obtained using STK 12.2, this study extracted and analyzed the time-series variation characteristics of the satellite semi-major axis and eccentricity before and after the two along-track impulsive maneuvers. The variation in the orbital semi-major axis is shown in Figure 10, the variation in orbital

eccentricity is shown in Figure 11, and the corresponding orbital element data are presented in Table 7. Since an along-track impulsive velocity increment can directly change the orbital energy of a satellite and further affect the orbital scale, mean motion, and orbital shape parameters, the semi-major axis and eccentricity exhibit orbital response characteristics corresponding to the maneuver epochs.

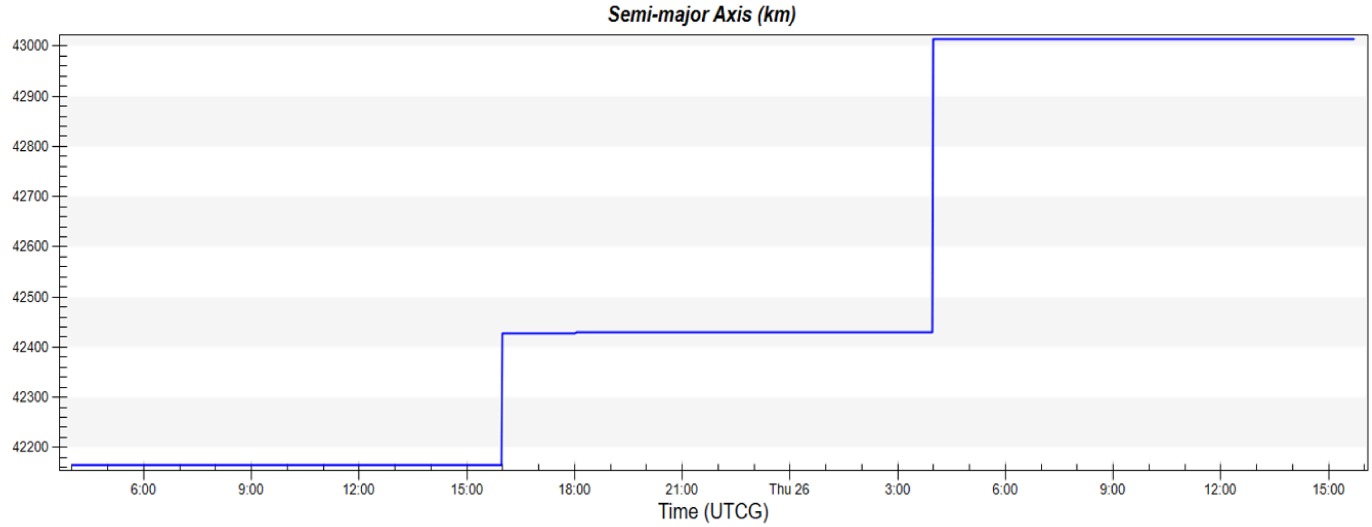


Figure 10. Variation in the semi-major axis of a high-orbit satellite after two maneuver events.

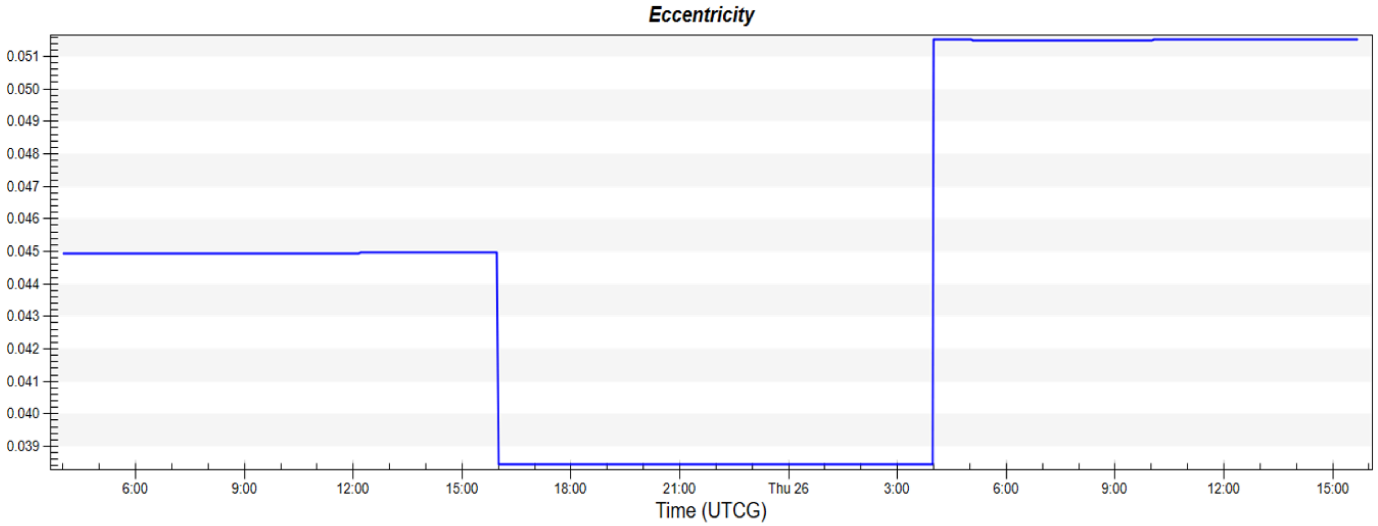


Figure 11. Variation in the eccentricity of a high-orbit satellite after two maneuver events.

Compared with LEO satellites, high-orbit satellites are less affected by atmospheric drag, whereas perturbation factors such as solar radiation pressure, the third-body gravitational effects of the Sun and Moon, and the Earth's nonspherical gravitational field have more pronounced effects on the long-term evolution of their orbital elements. Therefore, conducting maneuver simulations and analyzing orbital-element responses in high-orbit scenarios is important for distinguishing the gradual orbital variations caused by natural perturbations from anomalous orbital changes induced by maneuvers.

Based on the above orbit maneuver detection results for high-orbit satellites, when the orbital-element responses induced by along-track impulsive velocity increments are relatively pronounced, the satellite semi-major axis and eccentricity exhibit clear and distinguishable variations before and after the maneuvers. As a result, maneuver events can be effectively separated from the orbital evolution caused by natural perturbations. In

such large-amplitude orbit maneuver scenarios, the proposed orbit maneuver detection method can accurately identify the maneuver events, with an overall identification rate of 100%. This indicates that the proposed method exhibits good detection stability and reliability under significant maneuver conditions for high-orbit satellites.

Table 7. Partial variation in orbital elements of a high-orbit satellite after two maneuver events.

Time (UTCG)	Semi-Major Axis (km)	Eccentricity	Inclination (deg)	RAAN (deg)	Arg of Perigee (deg)	Mean Anomaly (deg)
25 March 2026 15:06:01	42,163.80	0.044953	28.486	359.992	0.009	166.96
25 March 2026 15:25:35	42,163.80	0.044952	28.479	359.993	0.005	171.868
25 March 2026 15:40:33	42,163.80	0.044952	28.485	359.991	0.002	175.624
25 March 2026 15:51:54	42,163.81	0.044952	28.478	359.991	0.001	178.472
25 March 2026 16:00:00	42,428.11	0.038443	28.483	359.992	359.917	180.584
25 March 2026 16:01:00	42,428.11	0.038443	28.482	359.993	359.917	180.832
25 March 2026 16:04:09	42,428.11	0.038443	28.482	359.993	359.916	181.617
26 March 2026 02:56:14	42,428.71	0.038432	28.501	359.986	359.892	343.589
26 March 2026 03:13:24	42,428.66	0.038432	28.502	359.985	359.896	347.848
26 March 2026 03:47:36	42,428.55	0.038430	28.501	359.986	359.905	356.333
26 March 2026 04:00:00	43,013.68	0.051510	28.501	359.984	359.753	359.565
26 March 2026 05:04:21	43,013.47	0.051504	28.503	359.986	359.766	15.211
26 March 2026 05:21:24	43,013.43	0.051502	28.502	359.987	359.769	19.359
26 March 2026 05:38:31	43,013.39	0.051513	28.502	359.988	359.772	23.519

To further evaluate the applicability, sensitivity, and robustness of the algorithm under low-amplitude maneuver conditions, ten high-orbit satellite orbit maneuver simulation scenarios were further constructed using STK. Several impulsive orbit maneuvers were applied to each satellite. All maneuvers were applied along the instantaneous velocity direction of the satellite, and the magnitudes of the impulsive velocity increments were randomly generated within the range of 0~10 m/s, so as to simulate the effects of along-track maneuvers with different intensities on the evolution of the orbital elements of high-orbit satellites. By statistically analyzing the orbital response characteristics under multi-target, multi-maneuver, and different velocity-increment conditions, the detection capability of the proposed method can be further examined when the amplitudes of orbital-element variations are relatively small and the distinguishability of maneuver features is reduced. This provides a more sufficient experimental basis for evaluating the engineering applicability of the algorithm in practical high-orbit satellite maneuver-monitoring tasks.

After determining the comprehensive criterion parameters for each target high-orbit satellite, it is necessary to further evaluate the applicability and stability of the selected parameter combination in high-orbit maneuver identification scenarios. Table 8 first presents the corresponding threshold-parameter settings for different high-orbit satellites, reflecting the parameter-selection characteristics of the comprehensive criterion method for high-orbit targets. Compared with LEO satellites, high-orbit satellites have longer orbital periods and smaller mean motions, and they are less affected by atmospheric drag. In contrast, perturbations such as solar radiation pressure, the third-body gravitational effects of the Sun and Moon, and the Earth's nonspherical gravitational field have more pronounced effects on the long-term evolution of their orbital elements. Figure 12 further summarizes the total number of data records, the number of anomalous records, the number of false detections, the number of missed detections, and the detection accuracy for each high-orbit satellite, thereby quantitatively evaluating the identification performance of the constructed comprehensive criterion system in high-orbit satellite maneuver detection tasks. The identifiers listed in the table are experimental IDs assigned in the simulation and are used solely to distinguish different simulated targets. Through statistical analysis of the multi-target detection results, the effectiveness of the proposed method in maneuver-feature extraction, anomalous-data discrimination, and adaptability to different high-orbit targets can be further verified. These results also provide experimental support for subsequent high-orbit satellite orbital anomaly monitoring and maneuver-behavior identification.

Table 8. High-orbit satellite IDs and threshold settings.

No.	Satellite ID	δ_1	δ_2	δ_3
1	41885	3.46	0.048	2.35
2	42915	4.12	0.053	2.58
3	43632	2.89	0.041	2.21
4	44757	5.28	0.062	2.91
5	45271	4.65	0.057	2.17
6	45920	6.17	0.068	2.42
7	46741	3.15	0.045	3.36
8	47682	5.74	0.060	2.73
9	48858	3.82	0.051	2.49
10	49127	6.93	0.074	3.22

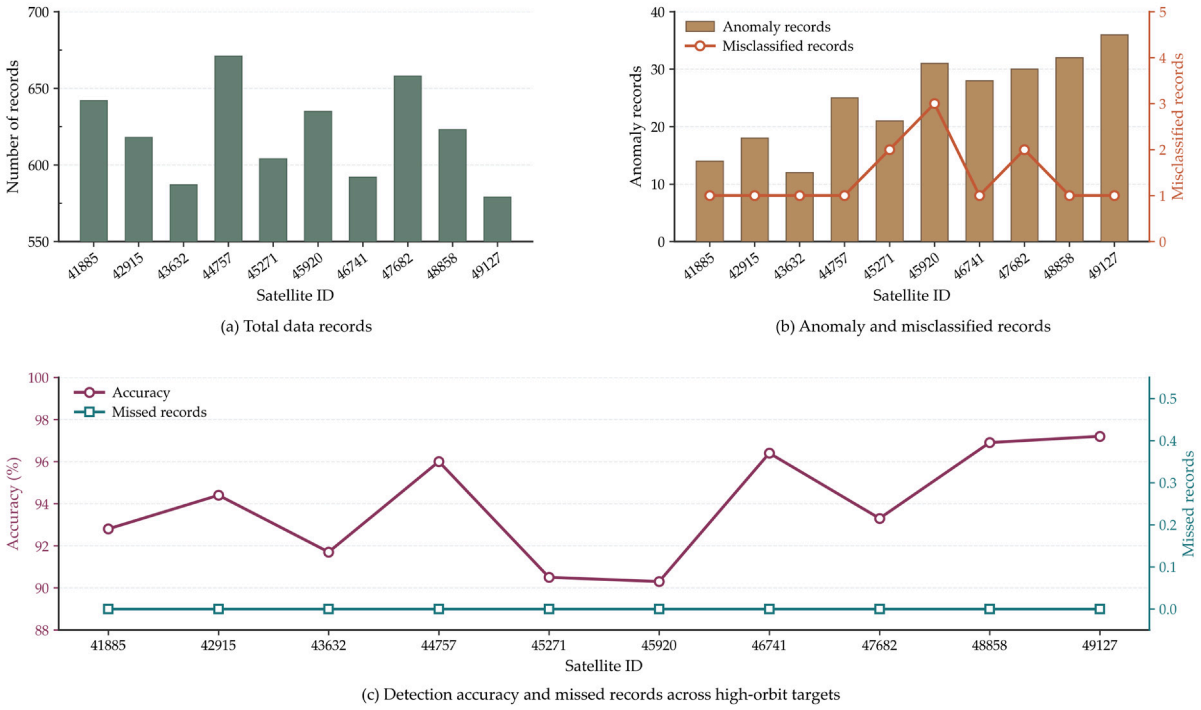


Figure 12. Orbit maneuver detection results for high-orbit satellites. (**a**) Total data records. (**b**) Anomaly and misclassified records. (**c**) Detection accuracy and missed records across high-orbit targets.

As shown in Figure 12, this study presents a statistical analysis of the orbit maneuver detection results for ten high-orbit satellites. Figure 12a shows the number of orbital data samples for each target. The number of samples for each satellite ranges from 579 to 671, with a total of 6209 samples, indicating that the experimental dataset is relatively balanced in scale and is suitable for evaluating the detection performance of the proposed method across different high-orbit targets. Figure 12b presents the number of data samples identified as anomalous for each satellite, together with the corresponding number of false alarms. A total of 247 anomalous samples are identified among the ten high-orbit satellites, accounting for 3.98% of the total dataset, while the number of false alarms is only 14, representing approximately 0.23% of all samples. Among the targets, satellite No. 49127 has the largest number of anomalous samples, with 36 detections, followed by satellites No. 48858, No. 45920, and No. 47682, with 32, 31, and 30 anomalous samples, respectively. Although the number of anomalous samples varies among different targets, the number of false alarms for each satellite remains within the range of 1–3, indicating that the proposed method retains effective false-alarm suppression capability under complex perturbation conditions

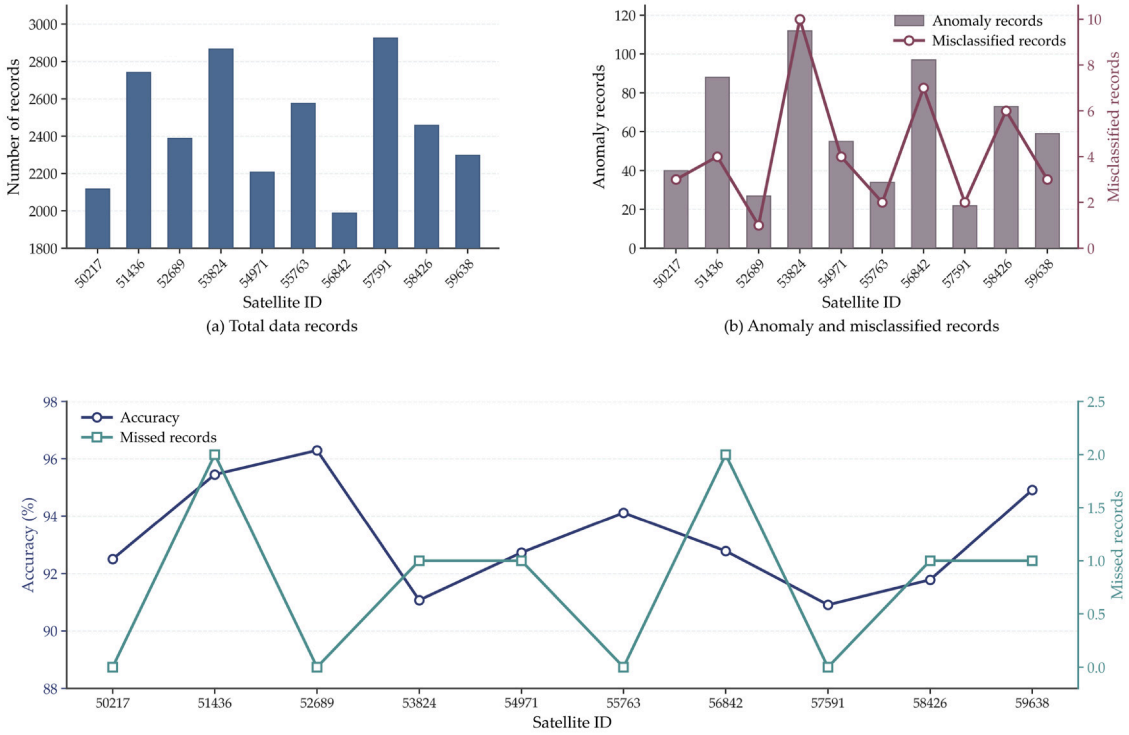
in high-orbit environments. Figure 12c shows the detection accuracy and the number of missed detections for each high-orbit target. The results indicate that the detection accuracy of individual satellites ranges from 90.3% to 97.2%, with an average accuracy of approximately 93.95%. Moreover, the number of missed detections is zero for all targets, demonstrating that the proposed method can successfully capture all known anomalous samples in this experimental dataset. Overall, the proposed algorithm achieves high detection accuracy, a low false-alarm ratio, and zero missed detections in high-orbit satellite orbit maneuver detection, thereby validating its stability and reliability for maneuver detection of high-orbit targets.

4.4.2. Radial Impulsive Maneuver Detection Experiment for High-Orbit Spacecraft

To further verify the applicability and generalization capability of the proposed method for detecting in-plane orbital maneuvers of high-orbit spacecraft under radial velocity increments, an independent high-orbit radial impulsive maneuver simulation scenario is constructed in this study. Different from the preceding high-orbit along-track maneuver experiment, another set of ten high-orbit spacecraft is selected as the experimental targets, and their catalog numbers do not overlap with those used in the along-track experiment, thereby avoiding dependence of the detection results on a specific target set. The semi-major-axis range of the selected targets is kept consistent with that in the preceding high-orbit experiment to ensure comparability in orbital altitude distribution. For each target spacecraft, orbit propagation is performed using the HPOP high-precision orbit propagator in STK 12.2. The perturbation force model, data output scheme, background noise estimation method, adaptive threshold calculation procedure, and multi-feature composite criterion are kept the same as those used in the preceding experiments. In the simulation, several radial impulsive orbital maneuvers are assigned to each high-orbit target. The magnitude of the radial velocity increment is randomly generated within the range of 0~10 m/s, and the maneuver direction is randomly selected between the positive and negative radial directions, so as to simulate the orbital evolution of high-orbit targets under weak radial velocity perturbations and different radial maneuver directions. To reduce the influence of boundary epochs and overlapping responses from adjacent maneuvers on the detection results, the maneuver epochs are set within the effective observation interval and are prevented from being too close to one another. During the detection process, the decision parameters are not readjusted for the high-orbit radial maneuver experiment; instead, the same parameter determination procedure as in the preceding experiments is adopted. To quantitatively evaluate the maneuver detection performance of high-orbit spacecraft under radial velocity increments, the total number of data records, number of anomaly records, number of false alarms, number of missed detections, and detection precision are used as statistical indicators. Figure 12 presents the detection results of ten high-orbit spacecraft under the radial impulsive maneuver scenario, which are used to further assess the anomaly-capturing capability, false-alarm suppression capability, and detection stability of the proposed algorithm for weak radial maneuver samples in high-orbit regimes.

As shown in Figure 13, this study presents a statistical analysis of the detection results for ten high-orbit spacecraft under the radial impulsive maneuver scenario. Figure 13a shows that the number of data samples for each target ranges from 1989 to 2926, with a total of 24,571 samples. This sample size is sufficient for evaluating the detection performance for high-orbit radial maneuvers, and the data volume varies non-monotonically among different targets. Figure 13b indicates that 607 anomaly records are identified in the radial impulsive maneuver scenario, accounting for 2.47% of the total samples, while 42 records are misclassified, representing 0.171% of all samples. Among the targets, spacecraft Nos. 53824, 56842, and 51436 have relatively large numbers of anomaly records, with 112, 97, and

88 records, respectively, suggesting that different high-orbit targets exhibit different orbital responses to radial velocity perturbations. Figure 13c presents the detection precision and the number of missed records. In this study, detection precision is used to evaluate the reliability of the identified anomaly samples, while the number of missed records is reported as an independent statistical indicator and is not included in the calculation of detection precision. The results show that the detection precision of individual targets ranges from 90.91% to 96.30%, with an average detection precision of 93.26%. The total number of missed records is 8, accounting for only 0.033% of all samples. Overall, the proposed method maintains high detection precision, a low misclassification ratio, and a low missed-detection level in the high-orbit radial impulsive weak-maneuver scenario, thereby validating its applicability and stability for detecting high-orbit radial in-plane maneuvers.



(a) Total data records

(b) Anomaly and misclassified records

(c) Detection accuracy and missed records across high-orbit radial-maneuver targets

Figure 13. Detection results for ten high-orbit spacecraft under radial impulsive maneuver scenarios: (**a**) total number of orbital data records for each target spacecraft; (**b**) detected anomaly records and corresponding misclassified records; and (**c**) detection accuracy and missed records across different high-orbit radial-maneuver targets.

4.5. Sensitivity Analysis of Key Empirical Parameters

To further verify the rationality of the empirical parameter selection in the proposed method, sensitivity analyses were conducted for two key parameters: the initial outlier-removal ratio p_{out} and the criterion-switching coefficient for nonuniform time intervals, γ, where $\Delta t \in [\Delta\bar{t}/\gamma, \gamma\Delta\bar{t}]$. The former affects the distribution of semi-major-axis difference samples used for background statistical modeling, whereas the latter determines the applicable time interval of the comprehensive criterion.

In the original configuration of the proposed algorithm, the samples are first sorted according to the magnitude of the semi-major-axis variation, and the top 5% of data points with the largest variations are removed to reduce the influence of TLE outliers and nonphysical spikes on background-noise estimation. Subsequently, for samples whose time intervals satisfy $\Delta t \in [\Delta\bar{t}/5, 5\Delta\bar{t}]$, the comprehensive criterion δ_i is adopted. For time

intervals that are significantly smaller or larger, the criterion is switched to $|\Delta a|$ and $|\Delta e/\Delta t|$, respectively. The main purpose of this design is to prevent a single component from being abnormally amplified in the comprehensive criterion due to nonuniform sampling, thereby improving detection stability.

To investigate the influence of the above parameters on detection performance, the overall algorithmic workflow and experimental samples were kept unchanged, while p_{out} and γ were varied separately. Comparative experiments were then conducted on both the LEO and high-orbit datasets. The LEO dataset contains ten satellites with a total of 25,662 orbital records, whereas the high-orbit dataset contains ten satellites with a total of 6209 orbital records. In this experiment, detection precision p, missed detection rate MDR, and false alarm ratio FAR were adopted as evaluation metrics. Detection precision is used to measure the proportion of true anomalous samples among the samples identified as anomalous. The missed detection rate is used to measure the proportion of true anomalous samples that are not identified, whereas the false alarm ratio is used to measure the proportion of normal samples that are incorrectly identified as anomalous. The formulas for calculating these metrics are given in Equations (28)–(30).

$$P = \frac{TP}{TP + FP} \times 100\% \tag{28}$$

$$MDR = \frac{FN}{TP + FN} \times 100\% \tag{29}$$

$$FAR = \frac{FP}{N_{normal}} \times 100\% \tag{30}$$

Among them, TP denotes the correctly identified maneuvers, FP denotes the number of normal samples incorrectly classified as anomalous, FN denotes the number of true anomalous samples that are not identified, and N_{normal} denotes the total number of normal samples.

First, a sensitivity experiment was conducted for the outlier-removal ratio. The initial outlier-removal ratio p_{out} directly affects the background statistical estimation of the semi-major-axis difference sequence. If p_{out} is too small, some TLE outliers or nonphysical spikes may still be included in the calculation of the mean and standard deviation, resulting in an overestimation of the background noise. This, in turn, raises the detection threshold and weakens the ability to detect weak maneuvers. If p_{out} is too large, high-amplitude samples associated with normal perturbation backgrounds may be excessively removed, leading to an underestimated statistical threshold and thereby increasing false alarms. Therefore, $p_{out} \in \{0\%, 1\%, 3\%, 5\%, 7\%, 10\%\}$ was selected for the parameter sensitivity experiment, with $p_{out} = 5\%$ adopted as the baseline setting.

For LEO targets, as shown in Figure 14a, when no initial outlier removal is performed, i.e., $p_{out} = 0\%$ the detection precision is only 90.80%, with a missed-detection rate of 3.10% and a false-alarm ratio of 0.180%. This indicates that abnormal spikes in the original TLE sequence interfere with the background statistics of the semi-major-axis differences, causing the threshold estimation to deviate from the true non-maneuvering background. When p_{out} increases to 5%, the detection precision improves to 94.42%, demonstrating that moderate initial outlier removal can effectively suppress the influence of abnormal samples on background modeling. However, when p_{out} further increases to 10%, the detection precision decreases to 92.80%, while the missed-detection rate and false-alarm ratio increase to 2.40% and 0.160%, respectively. This suggests that excessive outlier removal may damage the integrity of the background statistical samples and weaken the generalization capability of the detector.

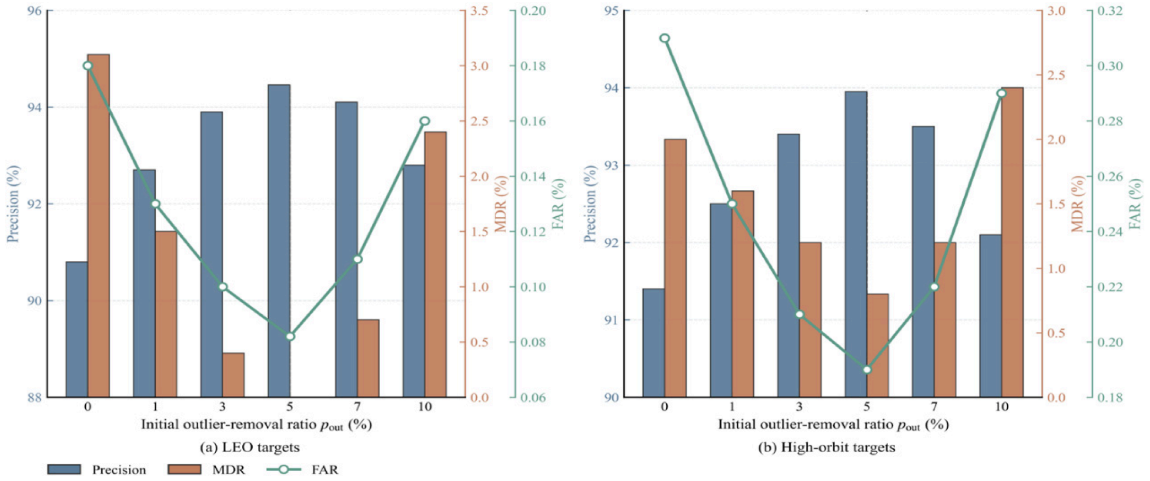


Figure 14. Sensitivity analysis of the initial outlier-removal ratio p_{out} for orbit maneuver detection. (**a**) LEO targets. (**b**) High-orbit targets.

For high-orbit targets, as shown in Figure 14b, the parameter variation trend is generally consistent with that of the LEO targets. When $p_{out} = 0\%$, the detection precision is 91.40%. When $p_{out} = 5\%$, the detection precision increases to 93.92%. When $p_{out} = 10\%$, the detection precision decreases to 92.10%, while the missed-detection rate and false-alarm ratio increase to 2.40% and 0.290%, respectively. Compared with LEO targets, high-orbit targets exhibit a higher overall false-alarm ratio, mainly due to the stronger effects of solar radiation pressure, third-body gravitational perturbations, and long-term perturbations.

Overall, the results for both LEO and high-orbit targets show that $p_{out} = 5\%$ provides a favorable balance across different orbital altitudes. It can reduce the influence of TLE outliers and local abnormal spikes on background noise estimation while avoiding statistical distortion caused by excessive removal of normal perturbation samples. Therefore, $p_{out} = 5\%$ is adopted as the initial outlier removal ratio in this study to balance detection precision, missed-detection control, and false-alarm suppression.

Next, a sensitivity experiment was conducted for the time-interval switching coefficient. The update intervals of TLE data are usually not strictly uniform. For samples with significantly large time intervals, the semi-major-axis variation may be anomalously amplified due to the time-accumulation effect. For samples with significantly small time intervals, the eccentricity variation rate may be amplified because of the excessively small denominator.

To prevent these situations from disrupting the balance among the three features in the comprehensive criterion, a time-interval switching coefficient γ was introduced. The applicable interval of the comprehensive criterion is written as $\Delta t \in [\Delta\bar{t}/\gamma, \gamma\Delta\bar{t}]$. When $\Delta t < \Delta\bar{t}/\gamma$, $|\Delta a|$ is used as the discrimination metric. When $\Delta t > \gamma\Delta\bar{t}$, $|\Delta e/\Delta t|$ is used as the discrimination metric. For the remaining samples, the comprehensive criterion δ_i is adopted. To verify the rationality of γ, $\gamma \in \{2, 3, 4, 5, 6, 8, 10\}$ was set in this experiment. Detection precision P, missed detection rate MDR, and false alarm ratio FAR were used as the evaluation metrics. The specific experimental results are shown in Figure 15.

As shown in Figure 15, the time-interval switching coefficient γ has a significant influence on the maneuver detection performance for both LEO and high-orbit targets. Overall, when γ increases from 2 to 5, the detection precision P of both types of orbital targets gradually improves, while the missed detection rate MDR and false alarm ratio FAR generally decrease. When γ is further increased to 8 or 10, the detection performance deteriorates, as indicated by decreased detection precision and increased missed detection rate and false alarm ratio. These results indicate that a larger time-interval switching

coefficient is not necessarily better. Instead, there exists an optimal trade-off between the applicable range of the comprehensive criterion and the suppression of errors caused by nonuniform sampling.

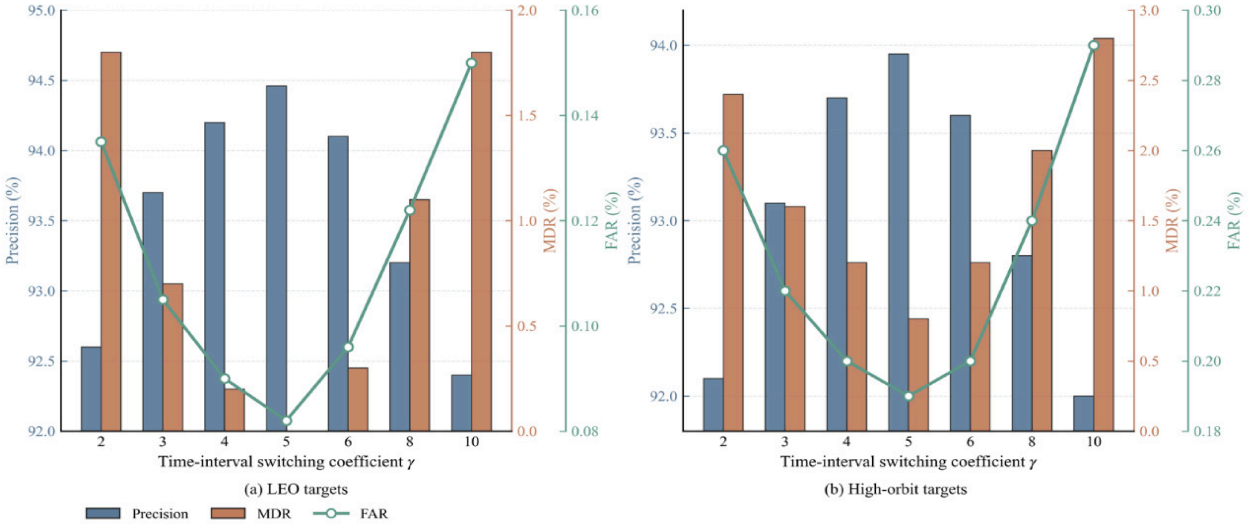


Figure 15. Effect of the time-interval switching coefficient γ on detection performance for LEO and high-orbit targets. (**a**) LEO targets. (**b**) High-orbit targets.

For LEO targets, as shown in Figure 15a, when $\gamma = 2$, the applicable interval of the comprehensive criterion is $[\Delta\bar{t}/2, 2\Delta\bar{t}]$, and the detection precision is 92.60%, the missed detection rate is 1.80%, and the false alarm ratio is 0.135%. In this case, the applicable range of the comprehensive criterion is relatively narrow. More samples are assigned to the short-interval or long-interval branches and are identified using a single criterion, which prevents the advantages of multi-feature fusion from being fully exploited. As γ increases to 5, the detection precision improves to 94.45%. This indicates that $\gamma = 5$ allows most samples with normal update intervals to enter the comprehensive-criterion processing stage, thereby making full use of the complementary information provided by the three features: semi-major-axis difference, eccentricity variation rate, and mean-motion dispersion.

When γ is further increased, the detection performance for LEO targets begins to degrade. For example, when $\gamma = 10$, the detection precision decreases to 92.40%, while the missed detection rate and false alarm ratio increase to 1.80% and 0.150%, respectively. This is because an excessively large γ broadens the applicable interval of the comprehensive criterion, causing some samples with significantly large or small time intervals to still be included in the comprehensive-criterion processing stage. For long-interval samples, $|\Delta a|$ may be amplified by the time-accumulation effect. For short-interval samples, $|\Delta e/\Delta t|$ may be amplified due to the excessively small denominator. Such scale imbalance among features caused by nonuniform sampling weakens the stability of the multi-feature criterion, thereby increasing the risks of false detections and missed detections.

The results for high-orbit targets show a trend consistent with that observed for LEO targets, as shown in Figure 15b. When $\gamma = 2$, the detection precision for high-orbit targets is 92.10%, the missed detection rate is 2.40%, and the false alarm ratio is 0.260%. When $\gamma = 5$, the detection precision increases to 93.96%. This indicates that the time-interval switching strategy is also applicable to high-orbit targets and can, to a certain extent, mitigate the effects of nonuniform sampling and complex background perturbations in high-orbit TLE sequences. However, compared with LEO targets, high-orbit targets generally exhibit higher false alarm ratios under different γ settings. This may be related to the stronger influence of solar radiation pressure, the third-body gravitational effects of the Sun and

Moon, and long-period perturbations on high-orbit targets. As a result, the background fluctuations in their orbital-element sequences are relatively more complex, making false-alarm suppression more challenging. When γ increases to 10, the detection precision for high-orbit targets decreases to 92.00%, while the missed detection rate and false alarm ratio increase to 2.80% and 0.290%, respectively. This further indicates that an excessively wide applicable interval for the comprehensive criterion weakens the corrective effect of the time-interval switching mechanism on anomalous sampling intervals, allowing nonuniform time-interval samples to adversely affect the comprehensive criterion. Therefore, for high-orbit targets, it is also necessary to reasonably constrain the applicable time range of the comprehensive criterion. Combining the experimental results for both LEO and high-orbit targets, $\gamma = 5$ provides relatively favorable detection performance for both types of orbital targets. The corresponding applicable interval of the multi-feature comprehensive criterion is $[\Delta\bar{t}/5, 5\Delta\bar{t}]$.

5. Conclusions

To address the difficulty of reliably identifying orbital maneuver signatures from publicly available TLE time-series data affected by natural perturbations, orbit-determination errors, outliers, and nonuniform update intervals, this study proposes a spacecraft orbital maneuver detection method based on an adaptive multi-feature criterion. By incorporating a dominant J_2 perturbation correction, the proposed method improves the dynamical consistency between the computed mean semi-major axis and the TLE mean-element framework. It further integrates semi-major-axis variation, eccentricity variation rate, and mean-motion dispersion to characterize maneuver-induced anomalous responses from three complementary perspectives: orbital energy, orbital shape, and motion frequency. In addition, the two-stage outlier-removal procedure, iterative background-noise estimation, and adaptive time-interval switching mechanism enhance the algorithm's adaptability to complex perturbation environments, anomalous noise, and nonuniform sampling.

Multi-target experiments involving both low-Earth-orbit and high-orbit satellites, together with parameter-sensitivity analyses, demonstrate that the proposed method can effectively detect in-plane orbital maneuvers dominated by along-track or radial velocity increments while maintaining good stability and robustness across different orbital altitudes, anomaly proportions, and perturbation conditions. Overall, the method combines physical interpretability, statistical robustness, and engineering applicability, providing technical support for spacecraft orbital anomaly monitoring and maneuver behavior identification based on publicly available orbital catalog data. Future work will extend the method to normal-direction maneuvers, continuous low-thrust maneuvers, and compound maneuver scenarios by incorporating additional orbital-plane features and multi-source observational information, with the aim of improving detection and parameter-estimation performance under more complex maneuver conditions.

Author Contributions: Conceptualization, S.Z., T.Z. and W.C.; Investigation, S.Z., T.Z. and W.C.; Methodology, S.Z. and T.Z.; Project administration, S.Z. and T.Z.; Supervision, S.Z., T.Z. and W.C.; Writing—review and editing, S.Z. All authors have read and agreed to the published version of the manuscript.

Funding: This research was funded by the National Key Laboratory of Space Target Awareness (STA2025KGJ0402).

Data Availability Statement: The datasets generated during the study are available from the corresponding author on reasonable request.

Conflicts of Interest: The authors declare no conflicts of interest.

Abbreviations

The following abbreviations are used in this manuscript:

SSA	Space Situational Awareness
TLE	Two-Line Element
LEO	Low Earth Orbit

References

1. Lemmens, S.; Krag, H. Two-Line-Elements-Based Maneuver Detection Methods for Satellites in Low Earth Orbit. *J. Guid. Control Dyn.* **2014**, *37*, 860–868. [CrossRef]
2. Li, T.; Chen, L. Historical-Orbital-Data-Based Method for Monitoring the Operational Status of Satellites in Low Earth Orbit. *Acta Astronaut.* **2018**, *151*, 88–94. [CrossRef]
3. Li, T.; Li, K.; Chen, L. New Manoeuvre Detection Method Based on Historical Orbital Data for Low Earth Orbit Satellites. *Adv. Space Res.* **2018**, *62*, 554–567. [CrossRef]
4. Bai, X.; Liao, C.; Pan, X.; Xu, M. Mining Two-Line Element Data to Detect Orbital Maneuver for Satellite. *IEEE Access* **2019**, *7*, 129537–129550. [CrossRef]
5. Clark, R.; Lee, R. Parallel Processing for Orbital Maneuver Detection. *Adv. Space Res.* **2020**, *66*, 444–449. [CrossRef]
6. Mukundan, A.; Wang, H.-C. Simplified Approach to Detect Satellite Maneuvers Using TLE Data and Simplified Perturbation Model Utilizing Orbital Element Variation. *Appl. Sci.* **2021**, *11*, 10181. [CrossRef]
7. Li, T.; Chen, L. Space Event Detection Method Based on Cluster Analysis of Satellite Historical Orbital Data. *Acta Astronaut.* **2019**, *160*, 414–420. [CrossRef]
8. Song, W.D.; Wang, R.L.; Wang, J. A simple and valid analysis method for orbit anomaly detection. *Adv. Space Res.* **2012**, *49*, 386–391. [CrossRef]
9. Shorten, D.P.; Humphries, M.; Maclean, J.; Yang, Y.; Roughan, M. Optimal Proposal Particle Filters for Detecting Anomalies and Manoeuvres from Two Line Element Data. *Acta Astronaut.* **2025**, *228*, 709–723. [CrossRef]
10. Zhang, H.; Zhao, C.; He, Z. Two-Line Element Outlier and Space Event Detection Method Based on Multi-Strategy Genetic Algorithm. *Appl. Sci.* **2024**, *14*, 3729. [CrossRef]
11. Liu, J.; Liu, L.; Du, J.; Sang, J. TLE Outlier Detection Based on Expectation Maximization Algorithm. *Adv. Space Res.* **2021**, *68*, 2695–2712. [CrossRef]
12. Liu, A.; Xu, X.; Xiong, Y.; Yu, S. Maneuver Strategies of Starlink Satellite Based on SpaceX-Released Ephemeris. *Adv. Space Res.* **2024**, *74*, 3157–3169. [CrossRef]
13. Gui, J.; Li, S.; Yang, B.; Diab, O. Satellite Maneuver Detection Using Dual-Moving Window Curve Fitting. *Acta Astronaut.* **2026**, *238*, 724–738. [CrossRef]
14. Huang, G.; Qin, Z.; Zhang, Q.; Wang, L.; Yan, X.; Fan, L.; Wang, X. A Real-Time Robust Method to Detect BeiDou GEO/IGSO Orbital Maneuvers. *Sensors* **2017**, *17*, 2761. [CrossRef] [PubMed]
15. Tu, R.; Zhang, R.; Fan, L.; Han, J.; Zhang, P.; Lu, X. Real-Time Detection of Orbital Maneuvers Using Epoch-Differenced Carrier Phase Observations and Broadcast Ephemeris Data: A Case Study of the BDS Dataset. *Sensors* **2020**, *20*, 4584. [CrossRef] [PubMed]
16. Qin, Z.; Huang, G.; Zhang, Q.; Le, W.; Xie, S.; She, H.; Lai, W.; Wang, X. The Analysis and Detection of Orbit Maneuvers for the BeiDou Satellites Based on Orbital Elements. *Acta Geod. Geophys.* **2021**, *56*, 501–522. [CrossRef]
17. Yu, S.; Wang, X.; Zhu, T. Maneuver Detection Methods for Space Objects Based on Dynamical Model. *Adv. Space Res.* **2021**, *68*, 71–84. [CrossRef]
18. Fan, L.; Tu, R.; Zhang, R.; Han, J.; Zhang, P.; Wang, S.; Hong, J.; Lu, X. An Orbit Maneuver Detection Method Based on Orbital Elements for BeiDou GEO and IGSO Satellites. *Adv. Space Res.* **2022**, *69*, 3644–3654. [CrossRef]
19. Song, W.; Li, C.; Dai, X.; Lou, Y.; Xu, Y. BDS near Real-Time Maneuver Detection Based on Triple-Differenced Phase Observations. *Adv. Space Res.* **2022**, *69*, 3032–3043. [CrossRef]
20. Qin, Z.; Zhang, Q.; Huang, G.; Tang, L.; Wang, J.; Wang, X. BDS Orbit Maneuver Detection Based on Epoch-Updated Orbits Estimated by SRIF. *Remote Sens.* **2023**, *15*, 2558. [CrossRef]
21. Zhang, W.; Zhang, K.; Li, X.; Zhao, Y.; Huang, J. Maneuver Detection and Estimation for LEO Real-Time Precise Orbit Determination with GNSS Observations. *GPS Solut.* **2025**, *29*, 103. [CrossRef]
22. Qiao, J.; Xu, H.; Li, B. Automatic Orbital Maneuver Detection and Thrust Model Establishment for Beidou GEO/IGSO Satellites. *GPS Solut.* **2026**, *30*, 80. [CrossRef]
23. Escribano, G.; Sanjurjo-Rivo, M.; Siminski, J.A.; Pastor, A.; Escobar, D. Automatic Maneuver Detection and Tracking of Space Objects in Optical Survey Scenarios Based on Stochastic Hybrid Systems Formulation. *Adv. Space Res.* **2022**, *69*, 3460–3477. [CrossRef]

24. Pastor, A.; Escribano, G.; Sanjurjo-Rivo, M.; Escobar, D. Satellite Maneuver Detection and Estimation with Optical Survey Observations. *J. Astronaut. Sci.* **2022**, *69*, 879–917. [CrossRef]
25. Porcelli, L.; Pastor, A.; Cano, A.; Escribano, G.; Sanjurjo-Rivo, M.; Escobar, D.; Di Lizia, P. Satellite Maneuver Detection and Estimation with Radar Survey Observations. *Acta Astronaut.* **2022**, *201*, 274–287. [CrossRef]
26. Montilla, J.M.; Sanchez, J.C.; Vazquez, R.; Galan-Vioque, J.; Benayas, J.R.; Siminski, J. Manoeuvre Detection in Low Earth Orbit with Radar Data. *Adv. Space Res.* **2023**, *72*, 2689–2709. [CrossRef]
27. Kaderali, S.; Misra, A. Detection and Characterisation of Unknown Maneuvers in Spacecraft. *Acta Astronaut.* **2023**, *205*, 310–318. [CrossRef]
28. Zhang, P.; Wu, D.; Baoyin, H. Real-Time Hybrid Method for Maneuver Detection and Estimation of Non-Cooperative Space Targets. *Astrodynamics* **2024**, *8*, 437–453. [CrossRef]
29. Montilla, J.M.; Vazquez, R.; Di Lizia, P. Maneuver Detection with Two Mixture-Based Metrics for Radar Track Data. *J. Guid. Control Dyn.* **2025**, *48*, 808–824. [CrossRef]
30. Yang, Z.; Huang, H.; Li, J.; Luo, Y. Spacecraft Maneuver Detection Based on Nonlinear Uncertainty Propagation along Decussated Orbital Arc. *Adv. Space Res.* **2025**, *76*, 2472–2487. [CrossRef]
31. Pirovano, L.; Armellin, R. Detection and Estimation of Spacecraft Maneuvers for Catalog Maintenance. *Acta Astronaut.* **2024**, *215*, 387–397. [CrossRef]
32. Wu, P.; Zhang, Y.; Li, J.; Chen, J. A Real-Time Maneuver Detection Method for Low Data Rate. *Acta Astronaut.* **2025**, *237*, 289–299. [CrossRef]
33. Long, X.; Leping, Y.; Weiwei, C.; Jinghong, L. GEO Spacecraft Maneuver Detection Based on Causal Inference. *Adv. Space Res.* **2023**, *72*, 3756–3769. [CrossRef]
34. Li, F.; Zhao, Y.; Zhang, J.; Zhang, Z.; Wu, D. A Station-Keeping Maneuver Detection Method of Non-Cooperative Geosynchronous Satellites. *Adv. Space Res.* **2024**, *73*, 160–169. [CrossRef]
35. Zollo, A.; Weigel, M. Comparison of Satellite Manoeuvre Detection Methods Based on Timeline of Orbit Elements. *Adv. Space Res.* **2024**, *73*, 286–303. [CrossRef]
36. Yang, S.; Jin, X.; Gong, B.; Han, F. Space-Based Passive Orbital Maneuver Detection Algorithm for High-Altitude Situational Awareness. *Aerospace* **2024**, *11*, 563. [CrossRef]
37. Peng, A.; Cui, B.; Huang, G.; Wang, L.; She, H.; Song, D.; Du, S. Real-Time Detection of LEO Satellite Orbit Maneuvers Based on Geometric Distance Difference. *Aerospace* **2025**, *12*, 925. [CrossRef]
38. Chen, H.; Pei, Z.; Wen, X.; Zhang, L.; Qiao, K.; Zhu, Z. Multi-Level Firing with Spiking Neural Network for Orbital Maneuver Detection. *Aerospace* **2025**, *12*, 991. [CrossRef]
39. Cipollone, R.; Frueh, C.; Di Lizia, P. LSTM-Based Maneuver Detection for Resident Space Object Catalog Maintenance. *Neural Comput. Appl.* **2025**, *37*, 17341–17362. [CrossRef]
40. Shi, G.; Pei, Z.; Chen, H.; Wang, J.; Song, C.; Chen, Y. Adaptive Spiking Gating Multi-Scale Liquid State Machine for Orbital Maneuver Detection. *Aerospace* **2026**, *13*, 417. [CrossRef]
41. Ai, J.; Hou, R.; Xiao, X.; Yang, Q. Impulsive Maneuver Detection with Radar Observation Using LSTM Neural Network. *IEEE Trans. Autom. Sci. Eng.* **2026**, *23*, 1701–1715. [CrossRef]
42. Rosengren, A.J.; Skoulidou, D.K.; Tsiganis, K.; Voyatzis, G. Dynamical Cartography of Earth Satellite Orbits. *Adv. Space Res.* **2019**, *63*, 443–460. [CrossRef]
43. Lara, M.; Fantino, E.; Flores, R. Orbital Perturbation Coupling of Primary Oblateness and Solar Radiation Pressure. *Nonlinear Dyn.* **2024**, *112*, 15073–15086. [CrossRef]
44. Srivastava, V.K.; Mishra, P.; Ramakrishna, B.N. Satellite Ephemeris Prediction for the Earth Orbiting Satellites. *Aerosp. Syst.* **2021**, *4*, 323–334. [CrossRef]
45. Di Carlo, M.; Graça Marto, S.D.; Vasile, M. Extended Analytical Formulae for the Perturbed Keplerian Motion under Low-Thrust Acceleration and Orbital Perturbations. *Celest. Mech. Dyn. Astron.* **2021**, *133*, 13. [CrossRef]
46. Armellin, R. Collision Avoidance Maneuver Optimization with a Multiple-Impulse Convex Formulation. *Acta Astronaut.* **2021**, *186*, 347–362. [CrossRef]
47. Zhang, G.; Mortari, D. Impulsive orbit correction using second-order Gauss's variational equations. *Celest. Mech. Dyn. Astron.* **2020**, *132*, 13. [CrossRef]
48. Xu, Y.; Zhang, Y.; Fan, L. Autonomous Semi-Major Axis Adjustment for Mega Constellation Continuous Coverage. *Adv. Space Res.* **2024**, *73*, 5582–5594. [CrossRef]

Disclaimer/Publisher's Note: The statements, opinions and data contained in all publications are solely those of the individual author(s) and contributor(s) and not of MDPI and/or the editor(s). MDPI and/or the editor(s) disclaim responsibility for any injury to people or property resulting from any ideas, methods, instructions or products referred to in the content.